

# A DEEP SEARCH FOR EXTENDED RADIO CONTINUUM EMISSION FROM DWARF SPHEROIDAL GALAXIES: IMPLICATIONS FOR PARTICLE DARK MATTER

KRISTINE SPEKKENS

Royal Military College of Canada, Department of Physics, PO Box 17000, Station Forces, Kingston, Ontario, Canada K7K 7B4

BRIAN S. MASON

National Radio Astronomy Observatory, 520 Edgemont Road, Charlottesville, VA 22903-2475

JAMES E. AGUIRRE

University of Pennsylvania, Department of Physics and Astronomy, 209 South 33rd Street, Philadelphia, PA 19104

BANG NHAN

Department of Astrophysical and Planetary Sciences, University of Colorado, 391 UCB, Boulder, CO, 80309  
*ApJ, in press*

## ABSTRACT

We present deep radio observations of four nearby dwarf spheroidal (dSph) galaxies, designed to detect extended synchrotron emission resulting from weakly interacting massive particle (WIMP) dark matter annihilations in their halos. Models by Colafrancesco et al. (CPU07) predict the existence of angularly large, smoothly distributed radio halos in such systems, that stem from electron and positron annihilation products spiraling in a turbulent magnetic field. We map a total of 40.5 deg<sup>2</sup> around the Draco, Ursa Major II, Coma Berenices, and Willman 1 dSphs with the GBT at 1.4 GHz to detect this annihilation signature, greatly reducing discrete-source confusion using the NVSS catalog. We achieve a sensitivity of  $\sigma_{sub} \lesssim 7$  mJy/beam in our discrete source-subtracted maps, implying that the NVSS is highly effective at removing background sources from GBT maps. For Draco we obtained approximately concurrent VLA observations to quantify the variability of the discrete source background, and find it to have a negligible effect on our results. We construct radial surface brightness profiles from each of the subtracted maps, and jackknife the data to quantify the significance of the features therein. At the  $\sim 10'$  resolution of our observations, foregrounds contribute a standard deviation of  $1.8 \text{ mJy/beam} \leq \sigma_{ast} \leq 5.7 \text{ mJy/beam}$  to our high-latitude maps, with the emission in the Draco and Coma dominated by foregrounds. On the other hand, we find no significant emission in the Ursa Major II and Willman 1 fields, and explore the implications of non-detections in these fields for particle dark matter using the fiducial models of CPU07. For a WIMP mass  $M_\chi = 100 \text{ GeV}$  annihilating into  $b\bar{b}$  final states and  $B = 1 \mu\text{G}$ , upper limits on the annihilation cross-section for Ursa Major II and Willman I are  $\log(\langle\sigma v\rangle_\chi, \text{cm}^3 \text{s}^{-1}) \lesssim -25$  for the preferred set of charged particle propagation parameters adopted by CPU07; this is comparable to that inferred at  $\gamma$ -ray energies from the two-year Fermi-LAT data. We discuss three avenues for improving the constraints on  $\langle\sigma v\rangle_\chi$  presented here, and conclude that deep radio observations of dSphs are highly complementary to indirect WIMP searches at higher energies.

*Subject headings:* galaxies: dwarf — dark matter — radio continuum: galaxies

## 1. INTRODUCTION

The standard cosmology derived from astronomical observations such as the cosmic microwave background, the large-scale galaxy distribution, and the kinematics of individual galaxies and clusters predicts that the universal matter density is dominated by dynamically cold, collisionless dark matter (e.g. Komatsu et al. 2011). Although there are few clues to its nature, its observed abundance requires that a dark matter particle have an annihilation cross section  $\langle\sigma v\rangle_{\chi,th} \sim 3 \times 10^{-26} \text{ cm}^3 \text{ s}^{-1}$  if it was once in thermal equilibrium (e.g. Porter et al. 2011). The correspondence of this cross-section to particles near the weak scale makes weakly interacting massive particles (WIMPs) very attractive dark matter can-

didates (see Jungman et al. 1996, Bergström 2000 and Feng 2010 for reviews). Whether WIMPs constitute the dark matter, and whether clues to the WIMP identity can be obtained are therefore pressing questions.

Indirect WIMP searches focus on detecting standard model particles that result from WIMP annihilations or decays. Given the relative paucity of astrophysical sources and the relative robustness of annihilation signature predictions at high energies,  $\gamma$ -ray searches have yielded some of the tightest constraints on  $\langle\sigma v\rangle_\chi$  (see Strigari 2012 for a recent review). A wide variety of objects have been targeted, including the Galactic center (e.g. Abdo et al. 2010a; Dobler et al. 2010; Abazajian & Harding 2012; Abazajian & Kaplinghat 2012; Weniger 2012), the diffuse Galactic and extragalactic backgrounds (Abdo et al. 2010c; Cirelli et al.

2010; Papucci & Strumia 2010; Baxter & Dodelson 2011; Ackermann et al. 2012a) and galaxy clusters (Ackermann et al. 2010; Abramowski et al. 2012; Ando & Nagai 2012; Han et al. 2012). However, uncertainties in astrophysical backgrounds, the dark matter distributions of the targeted systems and boost factors due to dark matter substructure weaken constraints derived from these studies (e.g. Su et al. 2010; Dobler et al. 2011; Inoue 2011; Ackermann et al. 2012a).

By contrast, nearby dwarf spheroidal galaxies (dSphs) are attractive targets for indirect dark matter searches: they are strongly dark matter dominated (e.g. Mateo 1998), and stringent upper limits on their star formation rates imply negligible astrophysical  $\gamma$ -ray emission (e.g. Ackermann et al. 2012b). In particular, the line-of-sight integrals of the squared dark matter distributions that are consistent with their stellar kinematics (the “J-values”) predict that the annihilation signal from Draco should be the strongest among the classical dSphs (Strigari et al. 2007; Charbonnier et al. 2011; Walker et al. 2011). J-values for the ultra-faint dSphs Ursa Major II (hereafter UMaII), Coma Berenices (hereafter Coma) and Willman 1 (hereafter Will1), while more uncertain, may be a factor of a few larger (Strigari et al. 2008; Strigari 2012). The basic optical properties of these four dSphs are given in Table 1.

Accordingly, many  $\gamma$ -ray experiments have targeted dSphs to search for WIMP annihilations (e.g. Abdo et al. 2010b; Ackermann et al. 2011; Aleksić et al. 2011; Aliu et al. 2012). No detections have been reported. The strongest upper limits on  $\langle\sigma v\rangle_\chi$  for WIMP masses  $M_\chi \lesssim 500$  GeV stem from observations with the Large Area Telescope (LAT) on Fermi (Atwood et al. 2009): analysis of the two-year Fermi-LAT data assuming  $M_\chi = 100$  GeV and annihilation into  $b\bar{b}$  produces upper limits  $\langle\sigma v\rangle_\chi \lesssim 10^{-25}$  cm<sup>3</sup> s<sup>-1</sup> for individual dSphs, and  $\langle\sigma v\rangle_\chi \lesssim 7 \times 10^{-26}$  cm<sup>3</sup> s<sup>-1</sup> when observations of 10 dSphs are combined (Ackermann et al. 2011; see also Geringer-Sameth & Koushiappas 2011).  $\gamma$ -ray searches are therefore closing in on  $\langle\sigma v\rangle_{\chi,th}$  expected for a thermal relic at these masses, though sensitivity gains of factors of a few are still required.

A variety of WIMP annihilation channels produce non-thermal electrons and positrons that could be detected when they lose energy through synchrotron, inverse Compton scattering or bremsstrahlung processes (see Profumo & Ullio 2010, for a review). Compared to  $\gamma$ -ray searches, this approach is complicated by uncertainties in charged particle propagation and energy losses. Nonetheless, because the expected signals span the electromagnetic spectrum and can be relatively sensitive to  $\langle\sigma v\rangle_\chi$ , a variety of multi-wavelength WIMP searches have been carried in the Galactic center (e.g. Bergström et al. 2006; Hooper et al. 2007; Crocker et al. 2010; Linden et al. 2010; Laha et al. 2012), the diffuse background (e.g. Hooper 2008; Fornengo et al. 2012; Hooper et al. 2012) and galaxy clusters (e.g. Pérez-Torres et al. 2009; Colafrancesco et al. 2006; Storm et al. 2012). In addition, radio (Tasitsiomi et al. 2004; Borriello et al. 2010; Siffert et al. 2011) and X-ray (Jeltema & Profumo 2008) observations of Local Group dwarf galaxies have been used to constrain WIMP properties in this context.

A series of models by Colafrancesco et al. (2007, here-

after CPU07) suggest that WIMP annihilations in Draco will produce a smoothly distributed, degree-scale radio synchrotron halo. Fig. 1 shows the predicted annihilation signal at  $\nu = 1.4$  GHz for a representative set of CPU07 models with  $M_\chi = 100$  GeV annihilating into  $b\bar{b}$  and a turbulent magnetic field strength in Draco of  $B = 1$   $\mu$ G. CPU07 adopt Milky Way-like diffusion models describing charged particle propagation of the form  $D(E) \propto D_0 E^\gamma$ , with either  $D_0 = 3 \times 10^{28}$  cm<sup>2</sup> s<sup>-1</sup> and  $\gamma = 1/3$  (“set #1”) or  $D_0 = 3 \times 10^{26}$  cm<sup>2</sup> s<sup>-1</sup> and  $\gamma = -0.6$  (“set #2”). Because the size of the diffusion zone corresponds to twice that of Draco’s stellar distribution, a crude estimate of the predicted annihilation halos for other dSphs is obtained by scaling the profiles radially according to their half-light radii  $r_h$  (Table 1). This approach assumes a fixed annihilation flux, which is reasonable given the similarity between the J-values of the systems considered here (Strigari et al. 2008; Strigari 2012). As discussed in §4.1.1, “set #2” is likely to be most appropriate for dSphs, with the model assumptions producing order-of-magnitude estimates of the predicted annihilation flux for a given  $\langle\sigma v\rangle_\chi$ .

Fig. 1 plots the predicted halo intensities for CPU07’s optimistic choice of  $\langle\sigma v\rangle_\chi \sim 3.4 \times 10^{-23}$  cm<sup>3</sup> s<sup>-1</sup>, a value that is now strongly ruled out by  $\gamma$ -ray searches. With this  $\langle\sigma v\rangle_\chi$ , the predicted signals would be easily detectable with existing single-dish radio telescopes. While CPU07’s  $\langle\sigma v\rangle_\chi$  is no longer relevant, realistic values of  $\langle\sigma v\rangle_\chi$  can be probed with the models of Fig. 1 by scaling them linearly in intensity when comparing to observations.

However, few strong constraints on the radio flux densities of dSphs exist (e.g. Fomalont & Geldzahler 1979), and no dedicated searches for extended radio halos in dSphs have been performed<sup>1</sup>. The dearth of extended emission searches in dSphs stems in part from the observational challenges associated with reaching sensitivities below the confusion limit of single-dish telescopes, imposed by discrete background sources (e.g. Condon 1974). Radio searches for WIMPs in dSphs therefore require a combination of single-dish observations to detect the predicted extended emission, and higher resolution interferometric observations to subtract discrete sources from the single-dish maps and beat their nominal confusion limit.

Accordingly, we have obtained deep radio continuum maps of dSphs using the Robert C. Byrd Green Bank Telescope (GBT) in order to search for extended radio halos resulting from WIMP annihilations. In this paper, we present  $\nu = 1.4$  GHz observations of degree-scale regions centred on Draco, UMaII, Coma and Will1. We subtract discrete sources from the Stokes I maps using the Karl G. Jansky Very Large Array (VLA) Sky Survey (NVSS; Condon et al. 1998) to reduce discrete-source confusion (§2.1 and §3.1), and confirm that discrete source variability is unimportant to our analysis with near-simultaneous VLA observations of the Draco field (§2.2 and §3.2). We find that our observations are

<sup>1</sup> Note that the limit for Draco from Fomalont & Geldzahler (1979) shown in fig. 12 of CPU07 has little relevance in the context of dark matter searches: these interferometric observations resolve out structures larger than few arcminutes and are therefore insensitive to degree-scale annihilation halos.

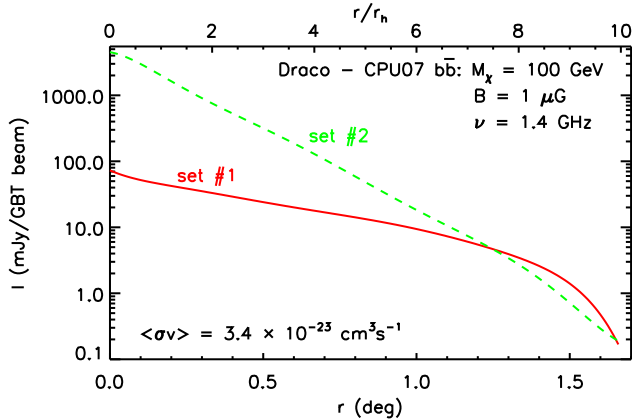


FIG. 1.— Predicted radial surface brightness profiles for Draco by CPU07, scaled to  $\nu = 1.4$  GHz and units of mJy per  $9.12'$  beam, appropriate for observations with the GBT at this frequency. The models assume  $M_\chi = 100$  GeV annihilating into  $b\bar{b}$  with  $\langle\sigma v\rangle_\chi = 3.4 \times 10^{-23} \text{ cm}^3 \text{ s}^{-1}$  (now strongly ruled out by  $\gamma$ -ray searches), and Milky Way-like diffusion models describing charged particle propagation of the form  $D(E) \propto D_0 E^\gamma$ , with either  $D_0 = 3 \times 10^{28} \text{ cm}^2 \text{ s}^{-1}$  and  $\gamma = 1/3$  (“set #1”) or  $D_0 = 3 \times 10^{26} \text{ cm}^2 \text{ s}^{-1}$  and  $\gamma = -0.6$  (“set #2”). The upper radial coordinate axis is expressed in units of the Draco half-light radius  $r_h$  (Table 1); we apply this model to other dSphs in our sample by scaling it radially to their  $r_h$ .

(A color version of this figure is available in the online journal.) foreground-limited (§2.1 and §4.2), and that foreground contamination precludes a detailed analysis of the Draco and Coma fields (§4.1.2). However, after accounting for the filtering of large-scale flux due to our baselining procedure (§3.3), we use non-detections in the UMaII and Will1 fields to place upper limits on  $\langle\sigma v\rangle_\chi$  in the context of the models shown in Fig. 1 (§4.1.1). We demonstrate that for a class of dark matter models like those of CPU07, deep radio observations are highly complementary to  $\gamma$ -ray searches for constraining the properties of particle dark matter (§4.1.1). We discuss the limitations of our analysis due to foregrounds (§4.2) and plausible magnetic field strengths in dSphs (§4.3), and describe an observational program to improve the limits on  $\langle\sigma v\rangle_\chi$  found here (§4.4).

## 2. OBSERVATIONS AND DATA PROCESSING

In order to search for extended radio halos in the dSphs in Table 1, we mapped  $1.5^\circ$ - to  $4^\circ$ -square regions centered on each dSph with the GBT at a frequency of  $\nu = 1.4$  GHz. This frequency affords the use of publicly available NVSS survey data to subtract discrete background sources. Below, we discuss the details of our GBT observations (§2.1) as well as our near-simultaneous VLA observations of the Draco field to assess the impact of discrete source variability in our final GBT maps (§2.2).

### 2.1. GBT Observations and Data Processing

Observations were made with the GBT in numerous observing sessions under the auspices of programs AGBT07C085 (for Draco) and AGBT09A085 (for UMaII, Coma, and Will1). Maps were made in the on-the-fly mode, scanning at  $104'$ /minute, with 2 seconds of integration time per pixel, giving a total time for one  $4^\circ \times 4^\circ$  map of 2.8 hours. The scan rate was chosen so that with the spectrometer backend integration time

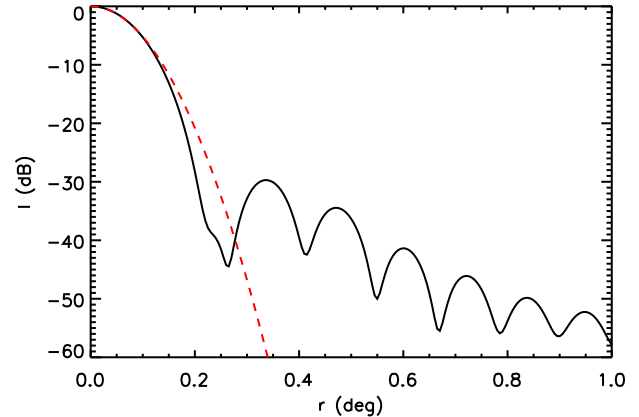


FIG. 2.— GBT beam model (solid line) at  $\nu = 1.4$  GHz used to convolve NVSS maps of each field to the GBT resolution in order to subtract discrete sources from each dSph field. Above a response of  $I = -7$  dB, the GBT beam is well-approximated by a Gaussian with a FWHM of  $9.12'$  (dashed line). (A color version of this figure is available in the online journal.)

of 1 second, the telescope motion is 20% of a beam full width at half maximum (FWHM) per integration, resulting in negligible beam smearing. RA and dec scans were interleaved to reduce the effect of  $1/f$  noise, either atmospheric or instrumental, on the final map. The GBT backends were configured to simultaneously record the receiver flux for all polarization products using both the Digital Continuum Receiver (DCR) and the GBT Spectrometer. The spectrometer produces both continuum and H I information. We defer a discussion of polarization and spectral data products to a future publication (J. Aguirre et al. 2013, in preparation). In this paper, we restrict our analysis to the two DCR XX and YY polarization channels, which, when averaged over parallactic angle (PA), approximate the continuum Stokes I intensity. The basic characteristics of the observations are presented in Table 2.

In order to search for extended halos for realistic values of  $\langle\sigma v\rangle_\chi$ , we need to reach sensitivities below the confusion limit of the GBT at  $\nu = 1.4$  GHz by subtracting discrete background sources (see §1). The  $45''$ -resolution NVSS provides a strong handle on this background. Note that although FIRST (Faint Images of the Radio Sky at Twenty Centimeters; Becker et al. 1995) boasts a higher angular resolution and sensitivity per beam than the NVSS, it has the significant disadvantage of resolving out smoothly distributed emission on angular scales larger than  $\sim 1'$ . We therefore subtract only sources detected by the NVSS. The GBT is sufficiently sensitive that NVSS sources are detected at high signal-to-noise in each individual  $\sim 10$ -second raster scan across a given map. In order to reduce cross-calibration uncertainties and to obtain a high-quality subtraction of the discrete sources using the NVSS, we directly calibrate the GBT data off of the latter.

For each scan, the raw GBT time-ordered data  $d(t_i) = d_i$  are modeled as

$$d_i = p_i + s \text{NVSS}_i, \quad (1)$$

where  $p_i$  is a first-order polynomial (mean and slope) to remove baseline drifts in the data,  $\text{NVSS}_i$  is the NVSS

TABLE 1  
BASIC PROPERTIES OF THE DSPH SAMPLE

Target	$(\alpha_0, \delta_0)$ (J2000)	$(l_0, b_0)$	$r_h$ (arcmin)	Reference
(1)	(2)	(3)	(4)	(5)
Draco	$17^{\text{h}}20^{\text{m}}14.4^{\text{s}} \pm 0.6^{\text{s}}, 57^{\circ}54'54'' \pm 08''$	$86.4^{\circ}, 34.7^{\circ}$	$10.0^{+0.3}_{-0.2}$	1
UMaII	$08^{\text{h}}51^{\text{m}}29.9^{\text{s}} \pm 4.0^{\text{s}}, 63^{\circ}07'59'' \pm 07''$	$152.5^{\circ}, 37.4^{\circ}$	$14.1 \pm 0.3$	2
Coma	$12^{\text{h}}26^{\text{m}}59.0^{\text{s}} \pm 0.9^{\text{s}}, 23^{\circ}54'27'' \pm 08''$	$241.9^{\circ}, 83.6^{\circ}$	$5.8 \pm 0.3$	2
Will1	$10^{\text{h}}49^{\text{m}}21.9^{\text{s}} \pm 0.8^{\text{s}}, 51^{\circ}03'10'' \pm 11''$	$158.6^{\circ}, 56.8^{\circ}$	$2.3^{+0.2}_{-0.4}$	1

NOTE. — Col. 2: RA and dec  $(\alpha_0, \delta_0)$  of the stellar dSph centroid; Col. 3: Galactic coordinates  $(l_0, b_0)$  computed from  $(\alpha_0, \delta_0)$ ; Col. 4: half-light radius of an exponential model of the stellar distribution; Col. 5: Reference: (1) Martin et al. (2008); (2) Muñoz et al. (2010).

template (in units of mJy per GBT beam) convolved to the GBT resolution, and  $s$  is a scale factor determined for each scan. Beam-maps constructed from scans across bright continuum sources show that the  $\nu = 1.4$  GHz GBT beam is well-approximated by a Gaussian with a FWHM of  $9.12'$  above  $-7$  dB, but that it falls off more rapidly than this at fainter levels. Our beam-maps are in good agreement with the GBT ray tracing model of Sri Srikant (priv. comm.); we therefore use an azimuthal average of this model, shown in Fig. 2, to convolve the NVSS data to the GBT resolution. Use of this more accurate model instead of a Gaussian significantly improves point source subtraction.

The values of  $p_i$  and  $s$  are determined by a least squares fit to the given scan’s data. We use a first-order polynomial for  $p_i$  as a compromise between removing  $1/f$  noise and not removing too much large-scale emission, and place quantitative limits on our sensitivity to extended halos in §3.3. The baseline-subtracted, NVSS-calibrated data  $D_i$  are then given by

$$D_i = (d_i - p_i)/s . \quad (2)$$

For conciseness, we refer to maps created from the  $D_i$  as “unsubtracted” because they contain discrete sources. By contrast, the baseline-subtracted, NVSS-calibrated and discrete source-subtracted data  $D_{sub,i}$  (which we will call “subtracted”) that we require for our analysis are given by

$$D_{sub,i} = (d_i - p_i - s NVSS_i)/s . \quad (3)$$

The subtracted scans were visually inspected for dramatic deviations from zero which could result from interference, atmospheric fluctuations due to poor weather conditions, or other problems; a small fraction of scans were rejected for these reasons. We also discard scans obtained at elevations below  $15^{\circ}$ , which is the case only in the Draco field. The remaining data had XX and YY polarizations combined to produce Stokes I, and gridded onto the sky using a standard cloud-in-cell method on a  $40''$  grid. The maps intended for visual inspection, and presented in Figs. 3–5, were constructed using a median gridding kernel in which the median of the integrations within a  $3 \times 3$  pixel box centered on each pixel is adopted as the final value. However, all computations were performed on maps constructed without median gridding, to ensure that the map weights were linearly propagated throughout the analysis.

The unsubtracted Stokes I GBT maps obtained from  $D_i$  for the four mapped fields are shown in the top row of

Fig. 3. All fields are plotted on the same angular scale, and are dominated by discrete sources. This is illustrated in Fig. 4 for Draco, which shows the inner  $2^{\circ} \times 2^{\circ}$  of the unsubtracted Stokes I GBT map and the NVSS map of the same region, convolved to the GBT resolution. The striking similarity between the discrete source patterns in the two panels suggests that source variability does not strongly affect our subtracted maps; we confirm this using near-simultaneous VLA observations in §3.2.

The second row in Fig. 3 shows the weight maps for the Stokes I data, which quantify the relative data contribution to each pixel on a linear scale from 0 to 1 (black and white in Fig. 3e–3h, respectively). All calculations performed include only map pixels whose weights exceed half the median value of the non-zero map weights. We verified that our results do not depend on the precise value of the median weight threshold adopted.

The third row in Fig. 3 shows “difference maps” for each field. The difference maps are a measure of mapping artifacts, which dominate the uncertainties in our analysis (see below). Specifically, we jackknife the data to produce three pairs of maps for each field created from only half of the collected data: that below (“Split A”) and above (“Split B”) the median time of observation, the median telescope elevation and the median telescope PA. The morphology of any real sky feature should be independent of these observing properties. Accordingly, for a perfectly mapped region Split A and Split B for each property would be identical, and subtracting Split B from Split A would produce a map containing no sky signal. We define our difference map as  $(\text{Split B} - \text{Split A})/2$ , so that the variance in these maps has the same scaling as that of Stokes I (because halves of the data are subtracted to produce the difference map). Note that finer data splits (e.g. into thirds) were also attempted, but the resulting maps were too noisy to be useful.

We therefore use the statistics of the features in the observed difference maps as a measure of the mapping errors. We create difference maps in time, elevation and PA for each field. In Fig. 3i–3l, we show the difference map for each field where the standard deviation of the pixels is the largest, and use this map for our error analysis in §3.1. For each field, the telescope property jackknifed to produce the plotted difference map is given in the bottom-left corner of the corresponding panel in Fig. 3: PA for Draco, UMaII and Coma, and elevation for Will1. As expected, the difference maps have more gaps than the Stokes I maps of Fig. 3a–3d, because a pixel must have data in each jackknifed half to be included in the



difference map.

The subtracted Stokes I GBT maps obtained from  $D_{sub,i}$  for the four mapped fields are shown in Fig. 5, and form the basis of our search for extended radio emission from the dSphs at each field center. Note that the upper colorscale limit in this figure an order of magnitude smaller than in Fig. 3a-3d: the vast majority of the detected flux in the unsubtracted maps stems from the discrete source population. Positive or negative features in the subtracted maps represent enhancements or depressions relative to the (positive) absolute sky brightness, which was subtracted during processing by virtue of  $p_i$  in equation (1).

There are no detectable residuals at the locations of the bright NVSS sources that were subtracted from the maps in Fig. 5, nor is there a correlation between the residual map emission and NVSS source locations. As a check, we repeat the analysis described in §3 by blanking regions within 1.5 GBT beams of bright NVSS sources: our results remain unchanged. Indeed, there are no discernible discrete source artifacts in our subtracted maps at all. This demonstrates that the NVSS is highly effective at reducing source confusion at the GBT resolution.

We quantify the sensitivity of the unsubtracted and subtracted GBT maps of each field in Table 3. As expected, the standard deviation  $\sigma_{usub}$  (col. 2) of the pixels in the unsubtracted Stokes I maps well exceeds the standard deviation  $\sigma_{sub} \lesssim 7$  mJy/beam (col. 3) in the subtracted maps. In turn, the values of  $\sigma_{sub}$  exceed the thermal noise expected from the radiometer equation by about an order of magnitude, as a result of both mapping errors and real sky variations. To disentangle the two, we use the statistics of the difference maps in Fig. 3i-3l. The estimated contribution of mapping uncertainties to the subtracted maps is  $\sigma_{map}$  (col. 4), and corresponds to the standard deviation of the pixels in the difference maps of Fig. 3i-3l. Assuming that the mapping and sky variances are additive,  $\sigma_{ast}$  (col. 5) is then the contribution to  $\sigma_{sub}$  from astrophysical sources. We discuss the interpretation of  $\sigma_{ast}$  as a measure of Galactic foregrounds in §4.2: in this context, Table 3 shows that our sensitivity is foreground-limited.

The final column in Table 3 is a measure of the dynamic range of the GBT observations, which we define as the ratio  $DR$  of the peak flux in the *unsubtracted* maps to the standard deviation  $\sigma_{sub}$  of the *subtracted* maps:  $DR$  is thus an indication of our ability to probe faint structures in the field after discrete source subtraction. We find  $DR \sim 140$  for the UMaII field, and note that the lower values for the other fields arise simply because the brightest continuum sources therein are fainter. Because we find no discrete source artifacts in any of the fields, we conclude that  $DR$  is only a lower limit to the dynamic range achievable for deep continuum observations with the GBT. Our discrete source subtraction is not an important contributor to the noise in the subtracted maps. It is therefore feasible to produce degree-scale, discrete-source subtracted GBT maps with sensitivities  $\sigma_{sub} \lesssim 7$  mJy/beam at 1.4 GHz, well below the nominal confusion limit.

## 2.2. VLA Observations and Data Processing

To constrain the variability of the discrete sources in the Draco field, we obtained VLA observations under

program AA315 on 2007 November 4, near the middle of the 3-month period over which the GBT data for this field were taken. The VLA was in B-configuration during that observing cycle, and we therefore configured the observing setup to match that of the FIRST survey, with one 7-channel, 3 MHz, dual-polarization frequency band centered at each of 1365 MHz and 1465 MHz. A comparison of the measured fluxes from our observations to the corresponding FIRST catalog entries provides a conservative upper limit on the variability in the NVSS sources in the same field, which we used for discrete source subtraction of the GBT data (see §3.2). A total of 5.4 hours were spent observing 110 snapshot pointings with the VLA in the Draco field, with flux calibrators observed at the start, middle and end of the observations and phase calibrators observed every 15-30 mins.

The mapping scheme was designed to reproduce the FIRST pointing grid in a  $4^\circ \times 4^\circ$  region centered on Draco, but an error in the interim VLA mapping software produced smaller pointing offsets than requested in RA. The final map therefore spans  $17^h 05^m 30^s < \alpha < 17^h 28^m 30^s$  and  $55^\circ 50' < \delta < 59^\circ 50'$ : this  $3^\circ \times 4^\circ$  region is centered on Draco in dec, but offset from it by  $\sim 0.5^\circ$  to the West. The basic characteristics of the observations are presented in Table 2.

The VLA data were reduced in AIPS (Greisen 2003). After interactively flagging bad baselines due to interference or poor instrumental performance, the flux calibrator was used to correct for the bandpass response functions of the antennas. The data were then flux and phase calibrated using standard AIPS routines, and the visibilities at 1365 MHz and 1465 MHz averaged. Each pointing was separately imaged and cleaned down to a residual noise level of 0.6 mJy, and then corrected for the geometric distortion produced by the VLA’s snapshot mode. The pointings were then mosaicked into a single, primary beam-corrected image.

Source fluxes in the VLA map were measured by fitting Gaussian components using the AIPS task JMFIT. To compare these measured fluxes to the corresponding FIRST catalog entries, we follow the procedure of de Vries et al. (2004): a) we cross-correlate the positions of our measured sources with those of the 08Jul16 FIRST catalog using a matching radius of  $3''$  (roughly half a synthesized beam), b) we compare the measured peak fluxes of unresolved, matched sources to that of their FIRST counterparts, restricting the comparison to sources brighter than 2 mJy (c.f. fig. 2 of de Vries et al. 2004). A total of 116 sources meet these criteria; we examined each one individually to ensure that none were unresolved components of a larger “parent” system.

Fig. 6 shows the distribution of (measured - FIRST) peak flux differences for the 116 sources. The flux differences are expressed in units of the net statistical uncertainty:  $\sigma_D = \sqrt{\sigma_m^2 + \sigma_F^2}$ , where  $\sigma_m$  is the uncertainty returned by JMFIT and  $\sigma_F$  is the RMS map noise at the source location listed in the FIRST catalog. Although we applied the FIRST clean bias correction to our measured fluxes (White et al. 1997), differences in absolute calibration and cleaning between the catalogs produced a non-zero median flux difference of 0.56 mJy. This has been subtracted from Fig. 6. The dotted line in the figure shows the best-fitting Gaussian to the distribution.

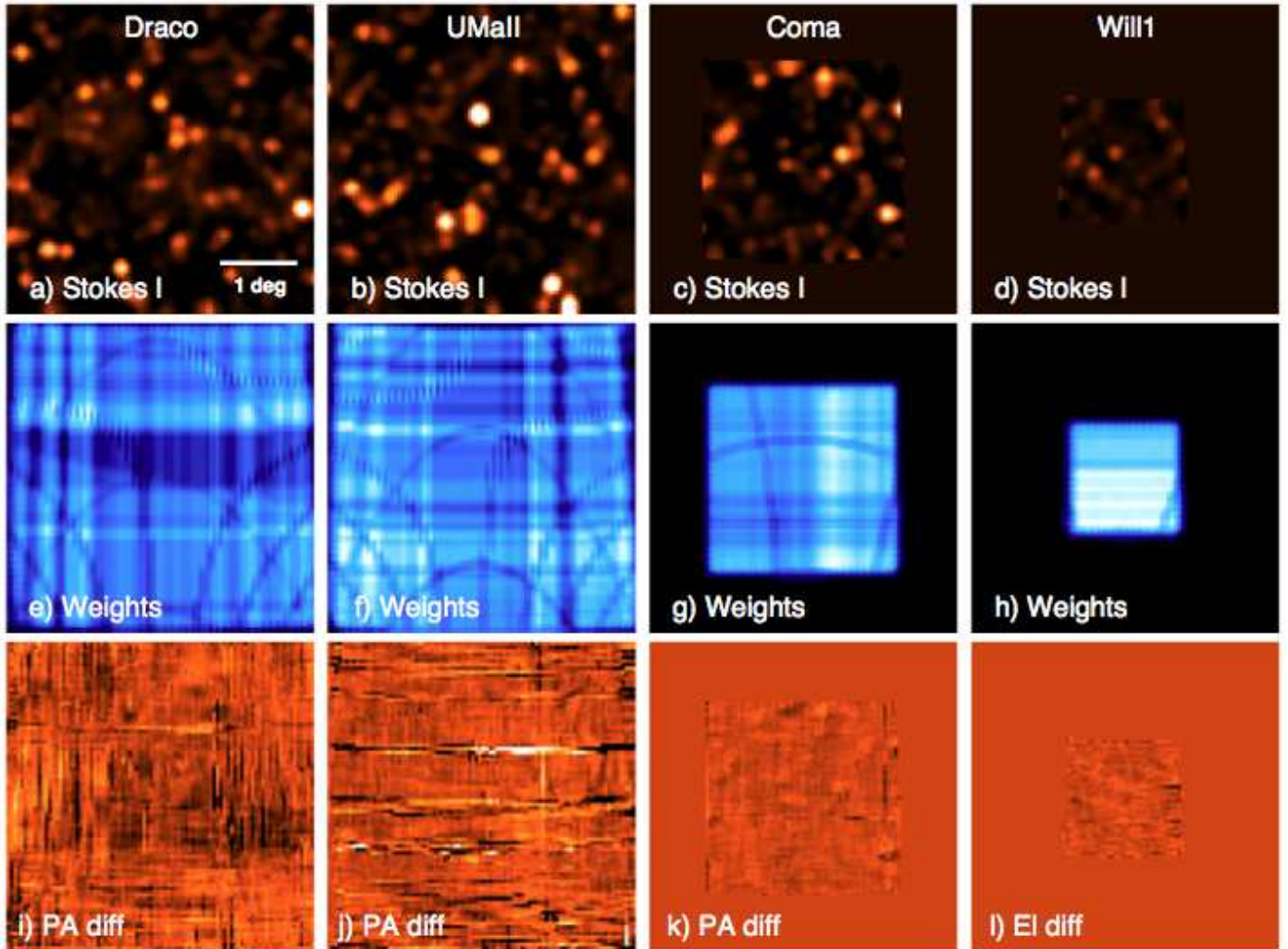


FIG. 3.— GBT data products. Each column corresponds to a distinct field that is labeled in the top row. All panels span  $4^\circ \times 4^\circ$ : the horizontal line in the bottom-right corner of a) shows an angular scale of  $1^\circ$ , and applies to all panels. The borders around the Coma and Will1 fields in the third and fourth columns are blanks around these smaller maps (see Table 2). *Top row*: Baseline-subtracted, NVSS-calibrated “unsubtracted” Stokes I maps of a) Draco, b) UMaII, c) Coma, d) Will1. The linear intensity scale ranges from -10 to 250 mJy/beam. *Middle row*: Weight maps for the Stokes I maps in the row above. The linear colorscale ranges from 0 (black) to 1 (white). *Bottom row*: Difference map, created by jackknifing the data, with the largest standard deviation for each field: i), j), k) PA, and l) elevation. The linear intensity scale ranges from -10 to 25 mJy/beam. (A color version of this figure is available in the online journal.)

TABLE 2  
OBSERVATION AND MAP PROPERTIES

Field (1)	Observing Dates (2)	Integ. Time (3)	Map Centre (4)	Dimensions (5)	Resolution (6)
Draco (GBT)	2007 October – December <sup>a</sup>	14.8 h	$17^{\text{h}}20^{\text{m}}, 57^\circ 55'$	$4^\circ \times 4^\circ$	$9.12' \times 9.12'$
UMaII (GBT)	2009 February – March <sup>b</sup>	18.8 h	$8^{\text{h}}52^{\text{m}}, 63^\circ 08'$	$4^\circ \times 4^\circ$	$9.12' \times 9.12'$
Coma (GBT)	2009 February – March	8.6 h	$12^{\text{h}}27^{\text{m}}, 23^\circ 54'$	$2^\circ.5 \times 2^\circ.5$	$9.12' \times 9.12'$
Will1 (GBT)	2009 February <sup>c</sup>	1.8 h	$10^{\text{h}}49^{\text{m}}, 51^\circ 03'$	$1^\circ.5 \times 1^\circ.5$	$9.12' \times 9.12'$
Draco (VLA)	2007 November 4	5.4 h	$17^{\text{h}}18^{\text{m}}, 57^\circ 53'$	$3^\circ \times 4^\circ$	$6.8'' \times 5.3''$

NOTE. — Col. 1: Field name. Instrument used to obtain the observations described in remaining columns is given in parentheses. Col. 2: Dates when majority of data were acquired. Col. 3: Total integration time for field. Col. 4: Map centre. Col. 5: Final map dimensions. Col. 6: Angular resolution of final map.

<sup>a</sup> 81% of data acquired during 2007 October – December; 19% acquired during make-up sessions in 2009 and 2010.

<sup>b</sup> 91% of data acquired during 2009 February – March; 9% acquired during make-up sessions in 2010 June.

<sup>c</sup> 74% of data acquired during 2009 February; 26% acquired during make-up sessions in 2010 June.

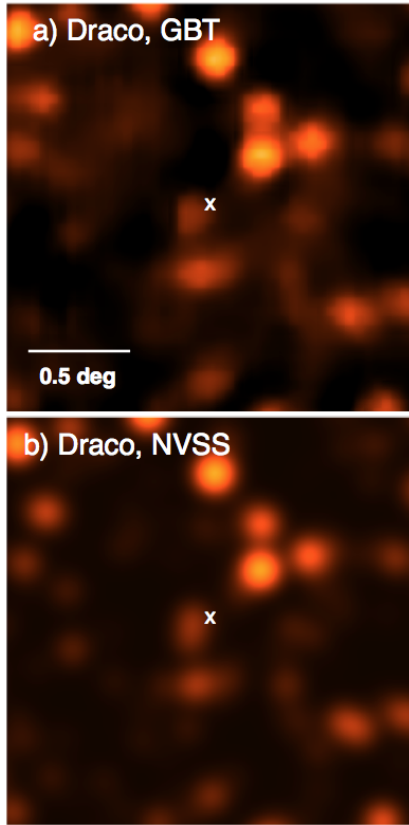


FIG. 4.— Comparison of the inner  $2^\circ \times 2^\circ$  of the Draco field from a) our GBT observations and b) the NVSS, convolved to the GBT resolution. The horizontal line in the bottom-left corner of a) shows an angular scale of  $0.5^\circ$ . In both panels, the linear intensity scale ranges from  $-10$  to  $250$  mJy/beam and the cross denotes the stellar centroid of Draco (Table 1). (A color version of this figure is available in the online journal.)

TABLE 3  
NOISE PROPERTIES OF THE GBT MAPS

Field	$\sigma_{usub}$ (mJy/bm)	$\sigma_{sub}$ (mJy/bm)	$\sigma_{map}$ (mJy/bm)	$\sigma_{ast}$ (mJy/bm)	DR
(1)	(2)	(3)	(4)	(5)	(6)
Draco	33	6.6	3.4	5.7	88
UMaII	50	6.3	5.1	3.7	142
Coma	34	3.6	1.3	3.3	87
Will1	14	2.3	1.5	1.8	37

NOTE. — Col. 1: Field name. Col. 2: standard deviation of pixels in unsubtracted map. Col. 3: standard deviation of pixels in subtracted map. Col. 4: estimated contribution to  $\sigma_{sub}$  in col. 3 from mapping uncertainties, or the standard deviation of the pixels in the difference map in Fig. 3i-3l. Col. 5: estimated contribution to  $\sigma_{sub}$  from astrophysical sources:  $\sigma_{ast}^2 = \sigma_{sub}^2 - \sigma_{map}^2$ . Col. 6: Dynamic range: ratio of peak brightness in unsubtracted map and  $\sigma_{sub}$ .

The vertical dashed lines denote  $\pm 4\sigma_D$ , which we adopt as our variability threshold.

We find that 7 unresolved, matched sources in our survey area exceed the  $4\sigma_D$  threshold, and thus exhibit variability on the  $\sim 10$ -year baseline probed by comparing our observations to the FIRST catalog; their properties are given in Table 4. The detected variable source density is in reasonable agreement with the results of de Vries et al. (2004), who use a similar catalog and ap-

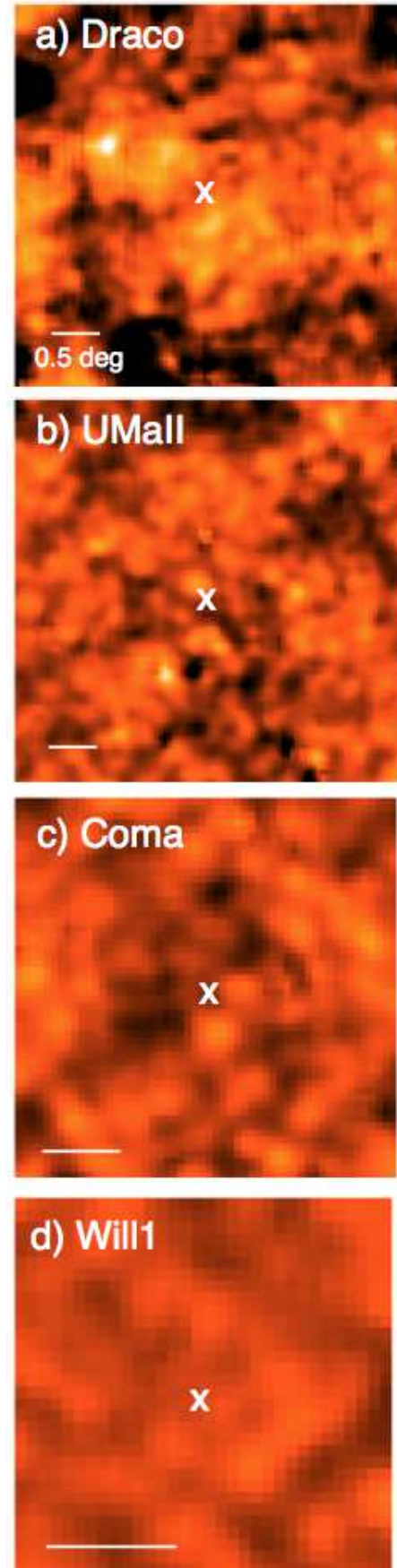


FIG. 5.— Discrete-source subtracted Stokes I maps of a) Draco, b) UMaII, c) Coma, d) Will1. The linear intensity scale ranges from  $-10$  to  $25$  mJy/beam: note that this upper limit is a factor of 10 smaller than that in Fig. 3a-3d. The horizontal line in the lower left corner of each panel is  $0.5^\circ$  in length, and the cross denotes the optical centroid of each dSph (Table 1). (A color version of this figure is available in the online journal.)



TABLE 4  
VARIABLE SOURCES IN THE DRACO FIELD

$\alpha, \delta$ (J2000) (1)	$F_F$ (mJy) (2)	$ F_m - F_F $ (mJy) (3)	$(\sigma_D)$ (4)	$FR$ (5)
17 <sup>h</sup> 05 <sup>m</sup> 04 <sup>s</sup> .5, 60°03′56″	3.76	1.81	4.53	1.48
17 <sup>h</sup> 19 <sup>m</sup> 37 <sup>s</sup> .3, 58°47′55″	27.3	7.18	25.2	1.36
17 <sup>h</sup> 27 <sup>m</sup> 50 <sup>s</sup> .7, 57°51′13″	2.03	1.40	5.43	1.69
17 <sup>h</sup> 08 <sup>m</sup> 02 <sup>s</sup> .3, 57°44′03″	4.32	1.94	7.22	1.81
17 <sup>h</sup> 06 <sup>m</sup> 50 <sup>s</sup> .1, 56°56′15″	4.33	2.08	5.81	1.92
17 <sup>h</sup> 25 <sup>m</sup> 45 <sup>s</sup> .7, 56°28′18″	7.24	1.22	4.15	1.20
17 <sup>h</sup> 06 <sup>m</sup> 57 <sup>s</sup> .4, 55°54′42″	3.54	1.20	4.08	1.34

NOTE. — Col. 1: FIRST source position. Col. 2: FIRST source peak flux. Cols. 3, 4: absolute (measured - FIRST) peak flux difference in mJy and in units of the net statistical uncertainty. The FIRST clean bias and median flux difference for the sample were subtracted. Col. 5: fractional variability, or the ratio of the brightest to the faintest flux ( $FR > 1$ ).

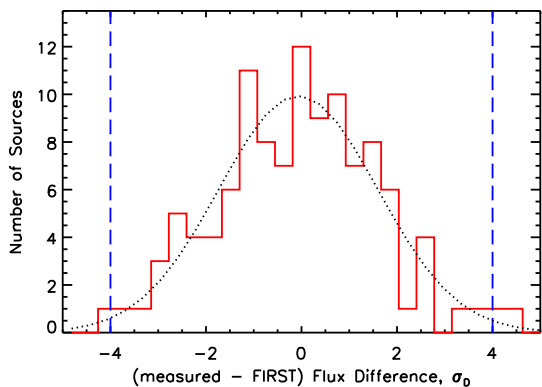


FIG. 6.— Difference between measured peak fluxes of unresolved sources in the Draco VLA field and FIRST catalog peak fluxes, expressed in units of the net measurement uncertainty  $\sigma_D$ . The dotted line shows the best-fitting Gaussian to the distribution, and the vertical dashed lines denote our variability threshold of  $4\sigma_D$ . (A color version of this figure is available in the online journal.)

proach to find 1 variable source per square degree over  $120.2 \text{ deg}^2$  of high-latitude sky on a 7-year baseline: 4/7 of our variable sources have a fractional variability below 50% (col. 5 of Table 4), while de Vries et al. (2004) report  $(73 \pm 4)\%$ .

We therefore conclude that on timescales of years, the variable source density and degree of discrete source variability in the Draco field is typical of that measured in other regions of the high-latitude sky. We investigate the impact of this variability on our search for an extended radio halo in Draco in §3.2.

### 3. SEARCHING FOR EXTENDED EMISSION

We wish to assess the likelihood that the subtracted Stokes I GBT maps in Fig. 5 contain emission that could constitute an extended dark matter annihilation halo. To quantify this, we compute the azimuthally averaged radial surface brightness profile in each GBT map relative to the stellar centroid of the dSph therein, as well as the statistical significance of features in the profiles (§3.1). We then establish that uncertainties due to variability in the discrete source populations subtracted from the maps have a negligible impact on the derived profiles

(§3.2). Finally, we quantify our ability to recover extended radio halo profiles given the baselining procedure adopted to calibrate the data (§3.3).

#### 3.1. Radial Profile Derivation

We carry out the bulk of our analysis on radial profiles computed from the subtracted Stokes I maps in Fig. 5. The reason for this is twofold. First, because the observations are dominated by mapping uncertainties (c.f. §2.1) it is difficult to characterize the noise in each pixel, which precludes computing reliable statistics directly from the maps. However, uncertainties on radial profile values can be robustly determined by jackknifing the data. Second, the CPU07 radio halo prediction is azimuthally symmetric (Fig. 1), and as a result the comparison of this prediction to profiles computed from the maps is straightforward.

We derive radial profiles  $I(r)$  from the subtracted Stokes I maps by extracting the mean value of all points that fall in circular rings as a function of distance from the stellar centroid of each dSph (Table 1). We note that the uncertainties on these centroids are much smaller than the resolution of our GBT maps, and varying the point about which the profile is computed within these uncertainties has no impact on the results.

We exploit the difference maps of each region to obtain realistic estimates of the uncertainties on each profile point  $I_i$ . We generate 5000 “shifted” realizations of each difference map: for each realization, we shift the map (and corresponding weights) by a random number of pixels in RA and dec, with pixels shifted outside the map region wrapped to the other side of it. We then compute the radial profile for each realization: for perfect data, this radial profile should have  $I(r) = 0$  regardless of the structure present in Stokes I. For each difference map, the uncertainty on each radial profile value  $I_i$  due to mapping errors is then the standard deviation of the points obtained from the 5000 realizations. We then adopt the uncertainties on the profile points derived from the difference maps in Fig. 3i-3l (that have the largest standard deviations for each field) as those on the profiles derived from the Stokes I maps.

Fig. 7 shows radial profiles derived from the subtracted maps in Fig. 5 (solid line), as well as those derived from the time (dotted line), elevation (dashed line), and PA (dash-dotted line) difference maps for each region. Qualitatively, all three difference map profiles for each field seem consistent with  $I(r) = 0$ , as expected if the telescope response has been properly calibrated out of the data and our error analysis is reliable. The profiles derived from the subtracted maps in the UMaII and Will1 fields (Figs. 7b and 7d) also seem to contain little structure. Conversely, the Draco profile (Fig. 7a) has  $I(r) > 0$  (relative to the subtracted mean sky brightness) at  $r < 1.3^\circ$ , while that for Coma (Fig. 7c) has  $I(r) < 0$  at  $r < 0.7^\circ$ .

We quantify the statistics of the radial profiles by computing the reduced  $\chi^2$  statistic for the hypothesis that  $I(r) = 0$ . We take into account correlated mapping uncertainties by using the covariance matrix derived from the profiles of the 5000 difference map realizations. Specifically, for each difference map  $j$ , the  $\chi_r^2$  statistic is



given by:

$$\chi_{r,C_j}^2 = \frac{1}{N} \mathbf{I}_j \mathbf{C}_j^{-1} \mathbf{I}_j^T, \quad (4)$$

where  $\mathbf{I}_j$  is a vector containing  $N$  radial profile points corresponding to that difference map,  $\mathbf{C}_j$  is the  $(N \times N)$  covariance matrix computed from the profiles of its 5000 realizations, and  $j$  is one of time, elevation or PA. The value of  $\chi_r^2$  for the Stokes I profile for each field is then obtained from:

$$\chi_r^2 = \min \left[ \frac{1}{N} \mathbf{I} \mathbf{C}_j^{-1} \mathbf{I}^T \right], \quad (5)$$

where  $\mathbf{I}$  is a vector containing  $N$  radial profile points from one of the Stokes I maps in Fig. 5. In words, we use the difference map covariance matrix that produces the smallest  $\chi_r^2$  to assess the significance of the features in each Stokes I profile. In practice, the  $\mathbf{C}_j$  used correspond to the difference maps shown in Fig. 3i-3l, whose pixel standard deviations are largest.

Table 5 shows  $\chi_r^2$  obtained for the discrete-source subtracted Stokes I maps and the difference maps for each region. For each entry, the number in parentheses is the one-sided  $p$ -value of the chi-squared test for that entry and the number of degrees of freedom in col. 2. Because the number of pixels contributing to each profile point increases with  $r$ , the outermost profile points strongly influence the reported statistics. We are most interested in quantifying detection statistics near each dSph at the centre of the maps, and therefore compute  $\chi_r^2$  for the profile points at smaller  $r$  than the vertical red arrow in each panel of Fig. 7; none of our conclusions change if all profile points in each field are included.

Table 5 confirms that there is no statistically significant structure in any of the difference maps for any field, and therefore that our calibration is effective and that the difference maps provide a reasonable estimate of the mapping uncertainties for each field. We note that the statistics of the difference map radial profiles change little if correlated errors are ignored in the analysis: the profile points are largely uncorrelated. Among the radial profiles for the discrete-source subtracted maps of each region, both Draco and Coma show statistically significant structure at the  $7.7\sigma$  and  $43\sigma$  level, respectively. As we discuss in §4, we attribute this structure to foregrounds. There is no statistically significant structure in the UMaII field, while that in the Will1 field is marginally significant at the  $5.8\sigma$  level.

### 3.2. Impact of Discrete-Source Variability

The similarity between the unsubtracted Stokes I maps and the NVSS data for each region (see Fig. 4 for Draco) and the absence of residuals at the locations of NVSS sources in our subtracted maps (Fig. 5) suggest that discrete-source variability does not strongly impact the derived radial profiles for each region. Below, we quantify this statement using the variability analysis for the Draco field from §2.2.

To estimate the importance of variability in the point-source population, we conservatively assume that the distribution of peak flux differences between our VLA map and the FIRST catalog (Fig. 6) for the Draco field stems entirely from intrinsic, low-level variability in the discrete source population on timescales of years, and that

this variability is present on the angular scales probed by the NVSS. In reality, one expects the variability of NVSS sources to be smaller than that of FIRST sources, because the extended radio emission resolved out by FIRST but retained by the NVSS typically varies on longer timescales than probed here. Simulations using the variability between our VLA observations and the corresponding FIRST map should therefore provide a conservative upper limit on the importance of this potential bias.

We therefore generate a new realization of the subtracted Stokes I GBT map for each dSph, and add a residual at the location of each NVSS source therein whose amplitude is randomly drawn from the gaussian in Fig. 6. The probability of drawing a  $\geq 4\sigma$  outlier from this distribution is much lower than required to produce the 7 genuinely variable sources in the Draco field (see Table 4): to account for this, we also assign the peak flux differences of these variable sources to 7 randomly selected NVSS source locations in each realization. We add these 7 sources to all of our fields, even those that are much smaller than the Draco field (Coma and Will1): this mimics the effect of a larger space density of variable sources, which we address below. The ensemble of residuals for each realization is convolved to the GBT resolution and added to the subtracted map for the corresponding field, and the radial profile is measured. We repeat this exercise 5000 times for each field to examine the variation in the measured profiles.

Fig. 8 shows the standard deviation  $\sigma_{Vi}$  at each profile point computed from the 5000 realizations in each of the mapped fields. For all  $r$  in all fields, these values are at least an order of magnitude smaller than the uncertainties on the radial profile points (c.f. Fig. 7):  $\sigma_{Vi} \ll \sigma_i$ . Even in the Coma and Will1 fields, where the space density of variable sources is assumed to be  $\sim 2.6$  and  $\sim 7$  times larger than in Draco by virtue of the addition of all 7 sources in Table 4, the resulting  $\sigma_{Vi}$  increases by at most 30%. It is clear that variability in the discrete source population contributes negligibly to the uncertainty in the measured radial profiles in Fig. 7.

The space density of bright ( $F \gtrsim 100$  mJy) transient or strongly variable radio sources is estimated to be  $\lesssim 0.004$  deg $^2$  (e.g. Gregorini et al. 1986; Croft et al. 2010; but see Matsumura et al. 2009), and they are therefore quite rare in degree-sized fields like those considered here. Nonetheless, it is possible for one such event to escape detection in our variability study (which only probed one  $\sim 10$ -year baseline) and produce a large residual in the discrete-source subtracted map. This scenario seems unlikely for our fields, since the largest residuals therein does not coincide with the location of NVSS sources. Nonetheless, we examined the impact of adding an unresolved residual, with an amplitude equal to the largest in the Draco field, at random locations in the subtracted Stokes I maps. Unless one is unfortunate enough to have this residual fall within  $\sim 2$  GBT beams of the profile center, this single large residual does not strongly alter the measured radial profiles. In practice, it is straightforward to mask out large residuals when the profile is computed, and we therefore consider the effect of this uncertainty to be negligible.

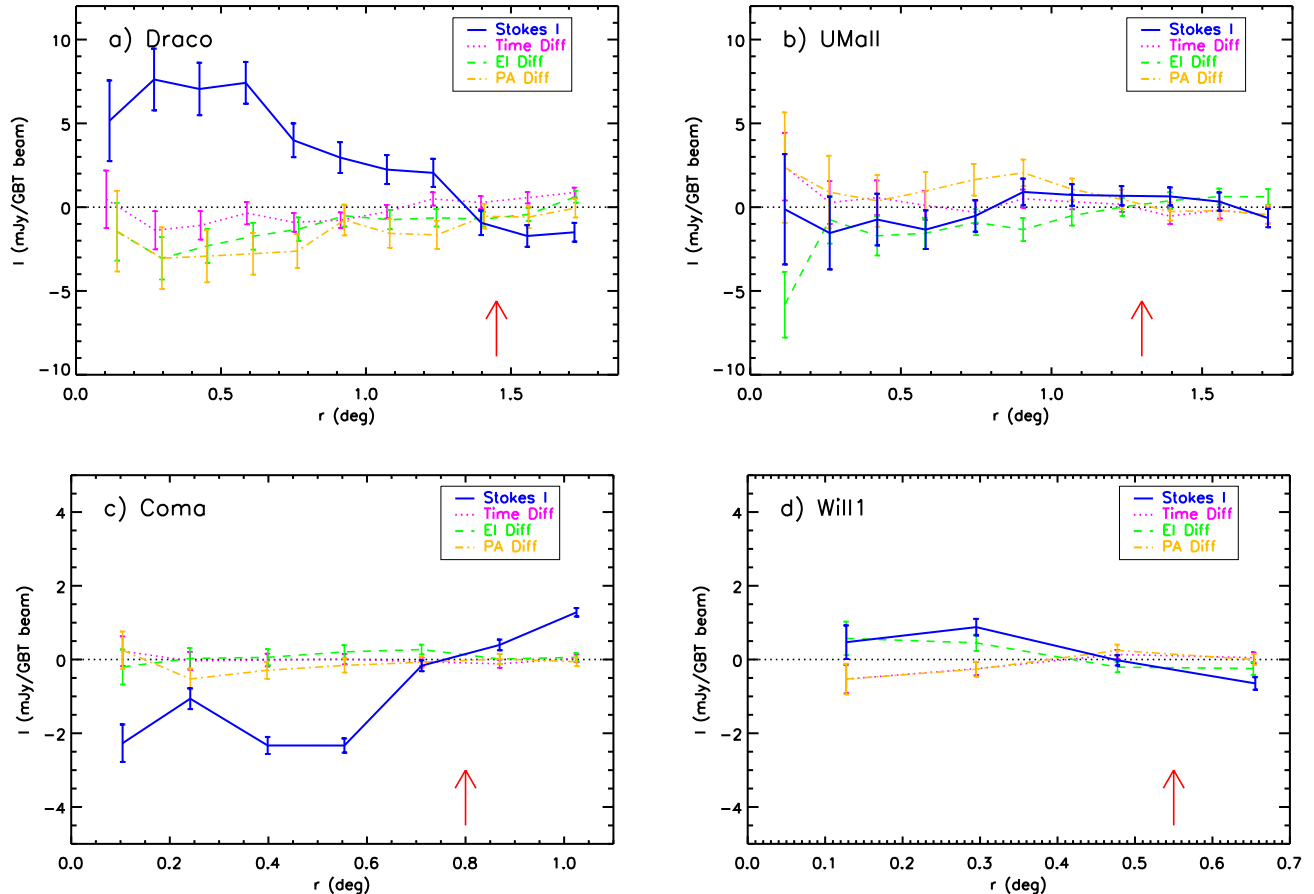


FIG. 7.— Radial profiles measured from the subtracted Stokes I GBT maps in Fig. 5 (solid line) for a) Draco, b) UMaII, c) Coma and d) Will1. Note that the horizontal and vertical scales in the panels differ. In each panel, the dotted, dashed and dot-dashed lines show profiles derived from the time, elevation and PA difference maps, respectively. For perfectly mapped fields, these profiles would have  $I(r) = 0$ . Points to the left of the vertical arrow were included in the  $\chi_r^2$  computation of Table 5 and the comparisons to the halo models of CPU07 in §4.1; see text for details.

(A color version of this figure is available in the online journal.)

TABLE 5  
RADIAL PROFILE  $\chi_r^2$  STATISTICS

Field (1)	DOF (2)	Stokes I (3)	Time Diff (4)	El Diff (5)	PA Diff (6)
Draco	9	7.7(<0.0001)	1.6(0.11)	1.1(0.36)	2.2(0.019)
UMaII	8	0.8(0.60)	2.1(0.032)	0.5(0.86)	1.0(0.43)
Coma	5	43(<0.0001)	1.1(0.36)	0.1(0.99)	1.1(0.36)
Will1	3	5.8(0.00078)	1.6(0.12)	1.3(0.27)	1.2(0.31)

NOTE. — Col. 1: Field name. Col. 2: Number of degrees of freedom in  $\chi_r^2$  computation. Cols. 3–6: Value of  $\chi_r^2$  obtained for the Stokes I (col. 3), time difference (col. 4), elevation difference (col. 5) or PA difference (col. 6) profile. The number in parentheses is the one-sided  $p$ -value of the chi-squared test given  $\chi_r^2$  and the degrees of freedom in col. 2.

### 3.3. Sensitivity to Extended Emission

A key step in processing single-dish radio continuum observations is the removal of baseline drifts in the data, which we parametrize with  $p_i$  in equation (1). Because these drifts have a characteristic scale on the order of the map size, an important side-effect of this step is that at least some large-scale emission is filtered out. This is a well-studied effect of the subtraction of poly-

nomial or other time-domain functions when making maps from time series scans (see also Dicker et al. 2009; Aguirre et al. 2011). We find that fitting a second-order polynomial to the data time-series is too aggressive, and filters out most of the annihilation halo flux predicted by CPU07. We have therefore implemented a linear baselining procedure, and evaluate its filtering effect here.

It is clear that the sensitivity of the final maps to a given emission feature is a function of both its character-

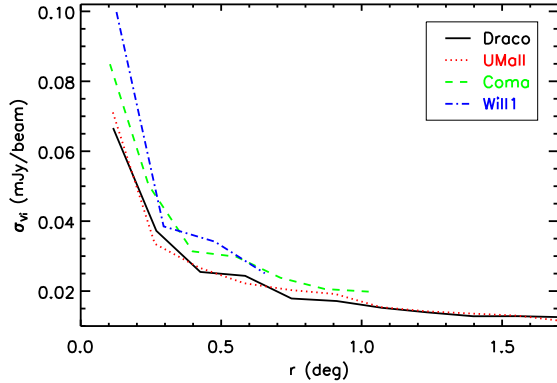


FIG. 8.— Estimated uncertainty in the discrete-source subtracted Stokes I profiles in Fig. 7 due to variability in the discrete source population. The lines show the standard deviation of profile points derived from 5000 realizations of the Draco (solid line), UMaII (dotted line), Coma (dashed line) and Will1 (dot-dashed line) fields obtained by adding residuals drawn from the Gaussian distribution in Fig. 6 as well as the 7 outliers from Table 4 randomly at the locations of NVSS sources. (A color version of this figure is available in the online journal.)

istic scale and morphology: to use the extremes as an example, our maps have full sensitivity to discrete sources but are blind to constant emission across the field, as the latter would be completely filtered out when the data are baselined. The most reliable way to quantify our sensitivity to extended halos is therefore to inject them directly into the time-ordered data and to attempt to recover them post-processing. We carry out this procedure as follows: we inject each of the profiles in Fig. 1, scaled radially to the  $r_h$  of the dSph in each field (Table 1), directly into the time-ordered data  $d_i$  to produce a “data+halo” input  $d_i + h_i$ . We then process  $d_i + h_i$  in the same manner as for  $d_i$  in §2.1. The maps produced from  $d_i$  are subtracted from those produced from  $d_i + h_i$ : to zeroth order, this eliminates thermal and mapping noise as well as the input  $d_i$  to produce an image of  $h_i$  after processing. Finally, we compute radial profiles from the processed  $h_i$  maps in the same manner as for the  $d_i$  for each field.

We verified that the reconstructed surface brightness of the processed halo images is linear with input halo surface brightness to within 2% for  $5 \text{ mJy/beam} < I < 100 \text{ mJy/beam}$ , as expected given the success of our discrete source subtraction [c.f. equation (1)]. We therefore produced processed images for a single “set #1” and “set #2” halo predicted by CPU07 for the dSph in each field.

Fig. 9 illustrates the impact of our processing pipeline on different input halos. The solid lines therein show “set #1” (Fig. 9a) and “set #2” (Fig. 9b) profiles evaluated at the measured profile radii for each of Draco, UMaII and Will1. For convenience, we normalize the innermost profile point to  $I_1 = 1 \text{ mJy/beam}$ . The dashed lines in the same color show the corresponding radial profile computed from the processed halo maps. As expected, our sensitivity to a given profile depends on its radial extent relative to the map size: for example, our processing pipeline recovers only  $\sim 60\%$  of the peak surface brightness for “set #1” in Draco, but almost all of the predicted “set #2” halo flux. Because a larger fraction of the “set #2” flux is recovered, we are corre-

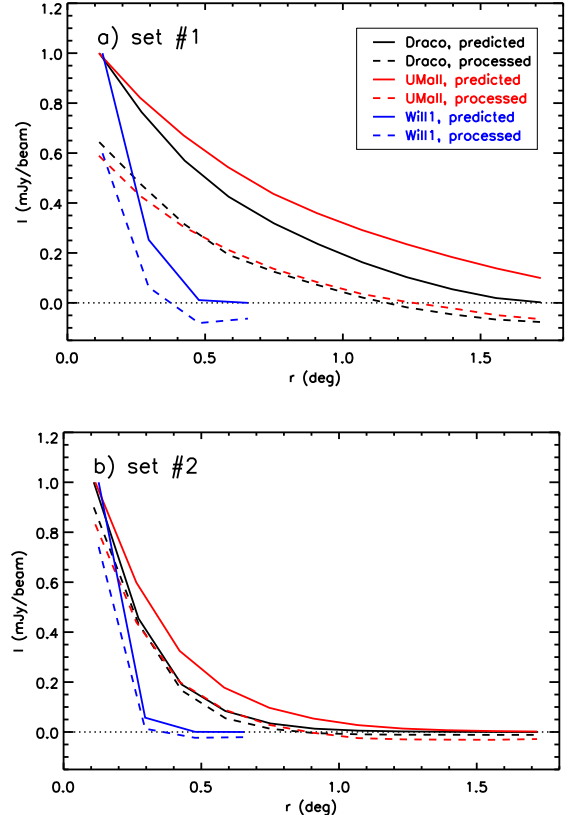


FIG. 9.— Impact of baselining procedure on CPU07 predictions for a) “set #1” and b) “set #2”. In each panel, the solid black, dark gray (red in the online version) and light gray (blue in the online version) lines show the predicted profiles from Fig. 1. The profiles are scaled radially to the  $r_h$  of the dSph of interest, evaluated at the measured profile radii of Fig. 7 and normalized so that the innermost profile point has  $I_1 = 1 \text{ mJy/beam}$ . The dashed lines of the same color show the profiles computed after processing the predictions through our pipeline, as described in §3.3. The processed profiles are both filtered and exhibit curvature bias, the extent of which depends on the angular size of the predicted halo. (A color version of this figure is available in the online version of the Journal.)

spondingly more sensitive to  $\langle \sigma v \rangle_\chi$  computed from this profile than for “set #1”: our maps will therefore yield a range of constraints on  $\langle \sigma v \rangle_\chi$  by virtue of the propagation parameters adopted.

Note that in Fig. 9, the processed “set #1” halo profiles are negative at large  $r$ : this is another artifact of the baseline subtraction. By removing a mean and slope from the maps, the linear baselining routine effectively imparts a “curvature bias” relative to the map center. Note, however, that this curvature bias does not imply a positive bias in large scale flux. The curvature bias could explain why the non-zero radial profiles for Draco and Coma, which we attribute to foregrounds below, appear to peak roughly at the map center. We explore mapping strategies to mitigate this and the filtering effect described above in §4.4.1.

Throughout this paper, we compare all data products to the processed halo profiles (c.f. Figs. 10 and 11) to account for any filtering or curvature bias due to our baselining procedure when placing constraints on the extended emission from the targeted dSphs.



#### 4. DISCUSSION: IMPLICATIONS FOR WIMPS AND FUTURE PROSPECTS

With measured radial profiles (§3.1), the impact of variability explored (§3.2) and an assessment of our sensitivity to extended radio emission in hand (§3.3), we turn now to the implications of the subtracted Stokes I maps for WIMPs. Specifically, we interpret our derived radial profiles in the context of the CPU07 predictions in §4.1, deriving upper limits on  $\langle\sigma v\rangle_\chi$  from the UMaII and Will1 fields (§4.1.1) and excluding WIMP annihilations as the source of the features in the Draco and Coma fields (§4.1.2). We devote §4.2 to a discussion of the limitations on our work imposed by foregrounds, and address the plausibility of invoking large-scale magnetic fields in dSphs in §4.3. In §4.4, we exploit the lessons learned in this study to suggest three avenues by which our constraints on  $\langle\sigma v\rangle_\chi$  can be improved and refined.

##### 4.1. Comparison to CPU07 Models

In order to provide an order-of-magnitude estimate of the  $\langle\sigma v\rangle_\chi$  that are probed by our maps, we compare the derived radial profiles in Fig. 7 to the fiducial CPU07 predictions shown in Fig. 1 (see §1). In §4.1.1, we derive upper limits on  $\langle\sigma v\rangle_\chi$  from the UMaII and Will1 profiles, and compare these limits to those obtained from the two-year Fermi-LAT data. In §4.1.2, we argue that the emission in the Draco field most likely stems from foregrounds rather than WIMP annihilations.

##### 4.1.1. Upper Limits on $\langle\sigma v\rangle_\chi$ from UMaII and Will1

The radial profiles in Fig. 7 and statistics of Table 5 show that there is no significant structure in the UMaII field, while that in Will1 is only marginally significant. These fields are thus devoid of both extended radio halos as well as significant astrophysical foregrounds (a fortuitous cancellation of these two components is very unlikely, as borne out by our analysis in §4.2.2). We therefore derive upper limits on the strengths of the radio halos in these dSphs allowed by the data: specifically, we assume that the emission from the dSphs in these fields is consistent with zero, and we use the errorbars on the profile points to derive upper limits on  $\langle\sigma v\rangle_\chi$ . We restrict ourselves to comparisons between our data and the fiducial CPU07 models shown in Fig. 1 to produce order-of-magnitude constraints on  $\langle\sigma v\rangle_\chi$ .

Fig. 10 shows the result of this exercise. The hatched regions in each panel show the uncertainties on our radial profile measurements, and the solid lines in each panel show the CPU07 “set #1” and “set #2” predictions – processed as described in §3.3 – normalized to be consistent with the profile uncertainties at 95% confidence. Because the outermost profile points pull strongly on the fit but are of little astrophysical interest, we include only points to the left of the vertical arrow each panel in the fit, as in the  $\chi_r^2$  computations of Table 5. The corresponding upper limits on  $\langle\sigma v\rangle_\chi$  are given on the right-hand side of the panel.

Fig. 10 illustrates that our upper limits on  $\langle\sigma v\rangle_\chi$  from UMaII and Will1 differ by at least an order of magnitude between the CPU07 “set #1” and “set #2”. This arises because the latter is more centrally concentrated than the former, which has two effects. First, for a given total flux, a centrally concentrated profile is easier to detect than

one distributed over more pixels. Second, our baselining algorithm filters out less flux for a centrally concentrated profile relative to a more extended one (see §3.3).

To compare our upper limits on  $\langle\sigma v\rangle_\chi$  with those from Fermi-LAT we first discuss the validity of the CPU07 diffusion models, which have the form  $D(E) \propto D_0 E^\gamma$  (see §1). The values of  $D_0$  adopted in CPU07’s “set #1” and “set #2” roughly span the  $\sim 3\sigma$  range allowed by cosmic-ray flux models of the Milky Way (Maurin et al. 2001; Donato et al. 2004). Scaling arguments from diffusion models of galaxy clusters suggest that  $D_0$  may be an order of magnitude smaller in dSphs than in the Milky Way, implying that “set #2” is most appropriate for dSphs (Jeltema & Profumo 2008). Although the CPU07 values of  $\gamma$  are significantly smaller than  $0.46 \lesssim \gamma \lesssim 0.85$  allowed for the Milky Way (Maurin et al. 2001), this parameter does not strongly affect the predicted annihilation flux at  $\nu = 1.4$  GHz (Jeltema & Profumo 2008). Recall that we scale the CPU07 profiles radially to account for different  $r_h$  of the dSphs (see Fig. 1), which also introduces uncertainty. Finally, we discuss plausible magnetic field values for dSphs in §4.3, and argue that  $B = 1 \mu\text{G}$  is a reasonable assumption. We therefore find the CPU07 “set #2” model to be plausible for dSphs, albeit with considerable uncertainty: the predicted annihilation flux is likely valid to within an order of magnitude.

Fig. 10 shows that comparing to the CPU07 models in Fig. 1, non-detections in the UMaII and Will1 fields imply and  $\langle\sigma v\rangle_\chi \lesssim 10^{-25} \text{cm}^3 \text{s}^{-1}$  for “set #2” at 95% confidence. For an identical decay channel, WIMP mass and statistical confidence, the two-year Fermi-LAT constraint for UMaII is  $\langle\sigma v\rangle_\chi < 2.17 \times 10^{-25} \text{cm}^3 \text{s}^{-1}$  (Ackermann et al. 2011); that for Will1 is not computed (c.f. Abdo et al. 2010b). Note that UMaII is the dSph for which the Fermi-LAT constraint is the tightest among the 10 dSphs in that study. Our upper limits on  $\langle\sigma v\rangle_\chi$  for the most plausible “set #2” diffusion parameters is therefore commensurate with those from the two-year Fermi-LAT data for individual dSphs.

We caution that a direct comparison between our limits and those from Ackermann et al. (2011) is muddled by several factors. Contrary to that study, we do not include J-value uncertainties in our upper limits. In addition, while random uncertainties due to foregrounds are encapsulated in the errorbars of Fig. 7, systematic uncertainties are not (see §4.2). Finally, we do not include (the considerable) uncertainties in the CPU07 diffusion models in our upper limits. All of these factors will weaken our constraints relative to those from Ackermann et al. (2011). On the other hand, the J-values for UMaII and Will1 are  $\sim 0.5 - 0.8$  dex larger than that implicit in the CPU07 models (Strigari et al. 2008; Ackermann et al. 2011): in this sense, our upper limits are conservative.

A suite of detailed, CPU07-like predictions tailored to UMaII and Will1 that will enable detailed comparisons between our limits on  $\langle\sigma v\rangle_\chi$  and those from Ackermann et al. (2011) is under construction (A. Natarajan et al, in preparation), but beyond the scope of the present work. Nonetheless, the comparisons of Fig. 10 indicate that deep radio observations of dSphs have the potential to provide interesting constraints on particle dark matter properties; as such, they are highly complementary to searches at  $\gamma$ -ray energies.

#### 4.1.2. Emission in the Draco Field

Fig. 7 and Table 5 illustrate that  $I(r) \neq 0$  in with high significance in the Draco and Coma fields. The depression near the Coma field center almost certainly stems from foregrounds, since an annihilation halo signal should be positive. However, the radial profile for Draco shows a statistically significant emission feature with the same basic morphology as that predicted by CPU07. However, two arguments suggest that this emission also stems from foregrounds instead of dark matter annihilation, and therefore that both the Draco and Coma fields are contaminated by foregrounds.

First, the subtracted Stokes I map in Fig. 5a exhibits a horizontal band of emission passing through the center of Draco, which is more suggestive of foregrounds than the expected symmetric emission centered on the dSph. Indeed, the amplitude of the emission seen in the Draco field is within a factor of two of the depression in the Coma field center, suggesting that the features in both maps stem from astrophysical foregrounds on similar angular scales. Recall that the correlation of these features with the map center stems at least in part from the curvature bias imparted by our baselining procedure (§3.3).

Second, there is tension between the  $\langle\sigma v\rangle_\chi$  implied by the Draco profile if foregrounds are negligible and the upper limits on this parameter from Fermi-LAT as well as from our UMaII and Will1 fields. Fig. 11 shows the best-fitting processed “set #1” and “set #2” predictions to the Draco profile points and the implied  $\langle\sigma v\rangle_\chi$ . It is clear that if one associates the majority of the emission in the Draco field with an extended halo, the  $\langle\sigma v\rangle_\chi$  required to produce the emission exceeds the Fermi-LAT two-year limits (Ackermann et al. 2011; Geringer-Sameth & Koushiappas 2011) and our UMaII and Will1 limits (Fig. 10). We therefore conclude that the Draco field is likely contaminated by foreground emission. We devote the next section to a thorough discussion of the limitations on our analysis due to foregrounds, and find that foregrounds cannot be reliably subtracted from the data in-hand; we therefore do not attempt to constrain  $\langle\sigma v\rangle_\chi$  from either the Draco or Coma fields.

#### 4.2. The Impact of Foregrounds

As explained in §4.1, our analysis of the derived radial profiles in the context of WIMPs is foreground-limited: we derive upper limits on  $\langle\sigma v\rangle_\chi$  from the UMaII and Will1 fields because they appear nearly foreground-free (§4.1.1), while we do not constrain  $\langle\sigma v\rangle_\chi$  from the Draco and Coma fields because they are contaminated by foregrounds (§4.1.2). We expand on the limitations due to foregrounds in this section. We discuss avenues for mitigating foregrounds in radio observations in §4.2.1, and argue that none can be reliably applied to the data in-hand. We therefore invert the problem in our maps to produce high-resolution, high-sensitivity measures of Galactic foreground emission at 1.4 GHz. In §4.2.2, we attempt to simultaneously disentangle annihilation halo and foreground signals using a joint Bayesian analysis of all four mapped fields: the results from this exercise validate our approach in §4.1.1.

##### 4.2.1. Mitigating Foregrounds

A potential avenue for mitigating Galactic foregrounds – which predominantly stem from synchrotron emission – is to explore the spectral dependence of the features in the subtracted maps of Fig. 5. The spectral index of the annihilation signature depends on the adopted propagation parameters (c.f. fig. 12 of CPU07), but it generally resembles  $\alpha \sim -0.7$  expected for Galactic synchrotron emission for  $1 \text{ GHz} \lesssim \nu \lesssim 10 \text{ GHz}$ , and steepens to  $\alpha \lesssim -1$  for  $10 \text{ GHz} \lesssim \nu \lesssim 100 \text{ GHz}$ . So in principle, deep  $\nu > 10 \text{ GHz}$  radio observations would enable spectral index analyses that may help to identify foregrounds and subtract them from the maps. In practice, however, mapping degree-scale fields at such high radio frequencies to the required sensitivity is prohibitively expensive.

We did attempt to examine extant survey data for the fields in Fig. 5 at lower frequencies from the compilation of diffuse Galactic radio emission by de Oliveira-Costa et al. (2008). Their predicted all-sky map at  $\nu = 1.4 \text{ GHz}$  is largely an extrapolation of the Haslam et al. (1982)  $\nu = 408 \text{ MHz}$  survey data, which has an angular resolution of  $1^\circ$  and an average zero-level uncertainty of 3 K. Processing these maps through our pipeline as described in §3.3, we find fluctuations on the order of 10 mJy/beam. However, scaling the Haslam et al. (1982) zero-point uncertainty to  $\nu = 1.4 \text{ GHz}$  assuming synchrotron foregrounds, these fluctuations lie well within the noise. There are therefore no extant foreground maps that have either the sensitivity or resolution to compare to our subtracted maps.

Another possibility for mitigating foregrounds is to use the Galactic H I spectral line signals that we collected simultaneously with the continuum measurements presented here (see §2.1; J. Aguirre et al. 2013, in preparation). H I is highly correlated with dust, which motivates the use of GBT-obtained H I maps to clean maps of Galactic foreground dust emission (Planck Collaboration et al. 2011). There is a correlation between the synchrotron and dust emission for entire galaxies which persists on very large scales, but the correlation on small scales is expected to be tight only for the highest radio frequencies (Bennett et al. 2003). Thus we do not expect that the H I emission will be a complete representation of foregrounds in our maps.

We can therefore turn the problem around and assume that there is no extended radio emission from any of the targeted dSphs; then, the maps in Fig. 5 provide a constraint on high-latitude Galactic foregrounds at unprecedented sensitivity and resolution. In particular,  $\sigma_{ast}$  in Table 3 is a measure of Galactic foregrounds at  $10'$  resolution and  $35^\circ \leq b \leq 84^\circ$ . We find  $1.8 \text{ mJy/beam} \leq \sigma_{ast} \leq 5.7 \text{ mJy/beam}$  for our fields with the largest  $\sigma_{ast}$  at the lowest  $b$  as expected. However, the correlation between  $\sigma_{ast}$  and  $b$  is not perfect, likely due to the small number of fields mapped. Nonetheless, our measurements represent an improvement of a factor of  $\sim 50$  in sensitivity and  $\sim 6$  in angular resolution over current foreground measurements at 1.4 GHz, such as that computed by de Oliveira-Costa et al. (2008).

##### 4.2.2. A Bayesian Halo and Foreground Estimate

The Draco and Coma fields were discarded from the analysis in §4.1 under the hypothesis that  $I(r) \neq 0$  therein stemmed from foreground contamination rather than extended radio emission. Although the foreground

argument seems to be the most plausible interpretation of the available data, it raises the uncomfortable possibility that  $I(r) \simeq 0$  in the UMaII and Will1 fields results from a fortuitous cancellation of a positive halo signal and negative foreground fluctuations: in this case our limits on  $\langle\sigma v\rangle_\chi$  have little meaning. We regard this scenario as unlikely but attempt here to simultaneously analyze all four mapped fields – allowing for a contribution to  $I(r)$  from both a CPU07 annihilation halo and a foreground contribution – in order to further validate the approach in §4.1.

We adopt a Bayesian approach using the best-fitting, processed CPU07 predictions to each Stokes I profile (as in Fig. 11 for Draco) and their uncertainties. We assume that the best-fitting intensities are drawn from a normal distribution with the following components: i) a positive definite annihilation halo signal, with a common normalization for all dSphs, ii) an RMS foreground signal which can be either positive or negative, and iii) our estimated zero-mean measurement noise. For the foreground signal we consider two cases: a) a foreground with constant RMS power across all fields, and b) a foreground with a  $1/\sin(b)$  dependence. We then find the most likely values of the halo normalization and the RMS foreground contribution given the best-fitting processed “set #1” and “set #2” profiles to the measured Stokes I profiles in Fig. 7 for all four fields jointly.

We find that the analysis strongly rules out the zero foreground case: it is not possible to interpret the Stokes I profiles from all four fields in the context of the CPU07 models without invoking a foreground contribution. This is not unexpected given  $I(r) < 0$  in the Coma field (Fig. 7c), but the analysis nonetheless lends some quantitative support to the approach adopted in §4.1. We find that an RMS foreground amplitude of 4–60 mJy/beam is allowed by the data at 95% confidence, with a most likely value of 6–9 mJy/beam. This estimate is consistent with  $1.8 \text{ mJy/beam} \leq \sigma_{ast} \leq 5.7 \text{ mJy/beam}$  obtained in §2.1, though with considerably larger uncertainty because an extended halo is simultaneously modeled and because the Bayesian estimate assumes only one foreground fluctuation in each map (on the scale of the annihilation halo signal), whereas  $\sigma_{ast}$  is computed over several independent beams. The most likely value of the halo normalization peaks near zero for both “set #1” and “set #2”, justifying our computation of upper limits on  $\langle\sigma v\rangle_\chi$  from the UMaII and Will1 profiles. However, including a foreground contribution weakens the upper limits on  $\langle\sigma v\rangle_\chi$  by  $\sim 0.5$  dex relative to those derived in §4.1 for both foreground models considered.

While the results of our Bayesian analysis are encouraging, we find that our sample of four dSphs is too small to meaningfully distinguish foregrounds from the signal of interest in a simultaneous fit: our approach in §4.1 of considering only fields that are unlikely to be contaminated by foregrounds is therefore preferable for the present study. Moreover, we have not considered the potential spatial dependence of the foreground signal within the maps, which is poorly constrained at their sensitivity and resolution (§4.2.1). Combined with the shortcomings of adopting a single halo normalization for all four fields, we find that a comprehensive Bayesian analysis is beyond the scope of this paper, but is likely to be both feasible and preferable as both larger samples and better models

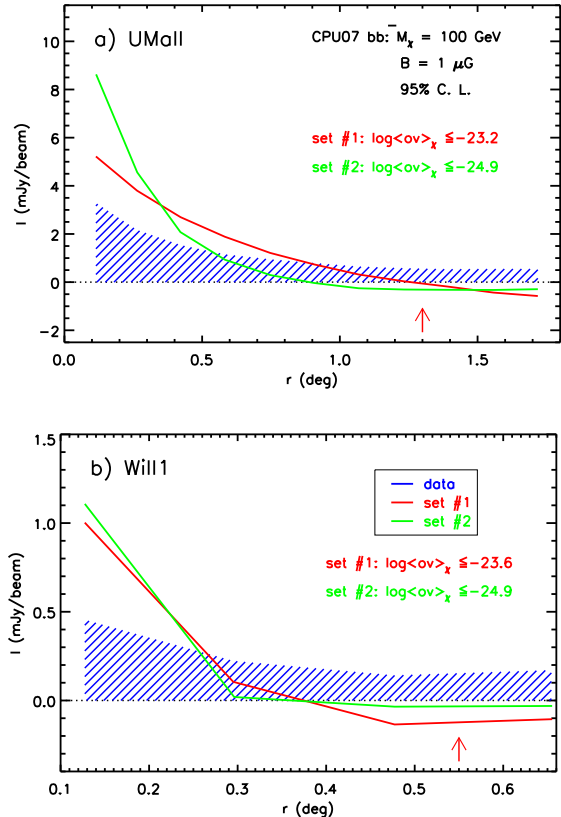


Fig. 10.— Upper limits on  $\langle\sigma v\rangle_\chi$  from a) UMaII and b) Will1 for the CPU07 models shown in Fig. 1, scaled radially using  $r_h$  for that dSph (Table 1). In both panels, the hatched (blue in the online version) region shows the radial profile uncertainties from Fig. 7. The black (red in the online version) and grey (green in the online version) lines show the CPU07 halo profile shapes for “set #1” and “set #2” respectively, processed through our pipeline to account for filtering by our baselining procedure and scaled in intensity to be consistent with the profile uncertainties at 95% confidence. Only uncertainties on profile points to the left of the vertical arrow are included in the fit.  $\log\langle\sigma v\rangle_\chi$  given on the right-hand side of the panels is the corresponding limit implied by the CPU07 models for a thermal relic, in  $\text{cm}^3\text{s}^{-1}$ . “Set #2” is likely to be most appropriate for dSphs (§4.1.1). (A color version of this figure is available in the online version of the Journal.)

become available (see §4.4).

### 4.3. Magnetic Fields in dSphs

Unlike their counterparts at  $\gamma$ -ray energies, WIMP annihilations in dSphs are detectable in the radio only if these systems harbor large-scale magnetic fields. CPU07 note that the dependence of the signal on the magnetic field strength is not trivial because it affects both the particle propagation and the synchrotron emission, but the sensitivity of their fiducial models scales roughly as  $\langle\sigma v\rangle_\chi \propto B$  (see their fig. 14). The magnetic field strength therefore has an important influence on the detectability of the predicted signal. Here we discuss the plausibility that the dSphs considered here have turbulent magnetic fields with strengths  $B \sim 1 \mu\text{G}$ , as assumed in the fiducial CPU07 models of Fig. 1.

Direct measurements of  $B$  are difficult to obtain (see Beck 2011, for a review). A standard technique is to search for radio emission attributable to synchrotron radiation, and to use the equipartition theorem to estimate



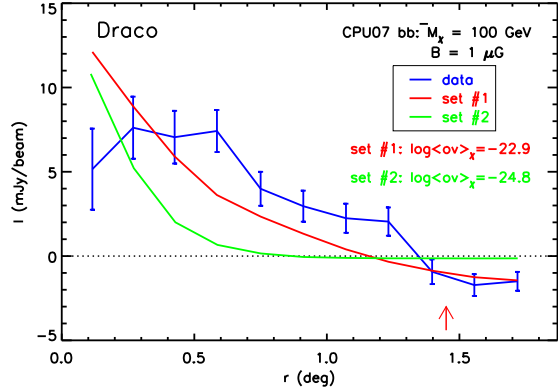


FIG. 11.— Best fitting processed “set #1” and “set #2” CPU07 predictions to the radial profile computed for the Draco field. The solid line with error bars shows the radial surface brightness profile points as in Fig. 7. The dotted black (red in the online version) and grey (green in the online version) lines show the best fitting “set #1” and “set #2” halo profiles, processed through our pipeline to account for filtering by our baselining procedure. Only profile points to the left of the vertical arrow are included in the fit. The corresponding  $\log\langle\sigma v\rangle_\chi$  is given on the right-hand side of the panels, in  $\text{cm}^3\text{s}^{-1}$ . Note that the detected emission likely stems from foregrounds and not WIMP annihilations; see text for details. (A color version of this figure is available in the online journal.)

the field strength. Under modest assumptions regarding the synchrotron spectral index and the degree of polarization, one can infer the total magnetic field strength. Using this approach, turbulent magnetic field strengths of  $\sim 10\ \mu\text{G}$  have been found in some actively star-forming, present-day dwarf irregular (dIrr) galaxies (Chyży et al. 2000, 2003; Kepley et al. 2010, 2011), while those in more quiescent systems like the LMC (Klein et al. 1989) are in the  $\sim 3 - 5\ \mu\text{G}$  range (see also Chyży et al. 2011). However, the lack of a detectable ISM precludes using this approach in present-day dSphs, and  $B$  therein is largely unconstrained.

In principle, an estimate of the line-of-sight integral of the magnetic fields and electron densities in dSphs can be obtained by measuring the Faraday rotation of the polarization angle of the polarized emission from background galaxies along the line-of-sight, i.e., the rotation measure. This has been done for the LMC (Gaensler et al. 2005), where they used polarized background galaxies with an areal density of 2.2 per square degree, measured with a sensitivity of 0.2 mJy/beam at 1.4 GHz. This magnetic field constraint underpinned the DM annihilation analysis of Siffert et al. (2011). Such a measurement could be done for dSphs, though it remains challenging. The most complete all-sky RM compilation (Oppermann et al. 2012) has about 1 source per square degree and reconstructs the RM field with a resolution of  $\sim 30'$ , with a high degree of non-uniformity, making it marginal for our purposes.

Notwithstanding the difficulties in measuring  $B$  in dSphs today, evidence for similar evolutionary histories between dIrrs and dSphs imply that the latter had magnetic fields in the past. The broadband photometric properties and resolved stellar populations of nearby dwarfs suggest that dIrrs and gas-poor dSphs had similar star formation histories until a few Gyr ago (Calura et al. 2008; Weisz et al. 2011). Numerical simulations indicate that “tidal stirring”, a combination of tidal and ram-

pressure stripping by the Milky Way halo, is effective at transforming dIrrs into (classical) dSphs (see Mayer 2010 for a review), again suggesting a common origin for these two classes. If dSphs and dIrrs share a common origin, then dSphs may once have had turbulent magnetic fields of order  $5 - 10\ \mu\text{G}$  as well. How this early magnetic field evolved after star formation ceased and their gas was stripped remains an open question.

It is nonetheless plausible that a tenuous, ionised ISM that has insofar escaped detection the dSphs sustains a weak magnetic field. For example, Draco could contain interstellar gas with a mass that is  $\sim 10\%$  of that in its stars and still satisfy available upper bounds on its diffuse  $\text{H}\alpha$  intensity (Gallagher et al. 2003). On the other hand, if we invoke equipartition in UMaII and Will1 and make standard assumptions regarding the synchrotron path length ( $l = r_h$  from Table 1) and the proton-to-electron ratio ( $K_o = 100$ ), the upper limits on the peak “set #1” and “set #2” flux densities in Fig. 10 would allow  $B \sim 1\ \mu\text{G}$  in these systems (Beck & Krause 2005). If the radio flux from low-luminosity galaxies is suppressed relative to that in  $L_*$  galaxies (e.g. Bell 2003),  $B$  could be larger. We conclude that although detailed modeling of the magnetic field evolution in dSphs is required to place quantitative limits on their most likely present-day strengths, it is plausible that these systems harbor a turbulent magnetic field with  $B = 1\ \mu\text{G}$  as invoked by CPU07.

#### 4.4. The Way Forward

Comparisons between the upper limits implied by the UMaII and Will1 surface brightness profiles and the preferred “set #2” CPU07 models in Fig. 1 require that  $\log\langle\sigma v\rangle_\chi \lesssim -25$  for each system, which rivals the constraints obtained by Fermi-LAT for individual dSphs (§4.1). It is therefore clear that deep radio observations of dSphs are highly complementary to WIMP searches at higher energies. We now discuss potential avenues for improving the constraints on  $\langle\sigma v\rangle_\chi$  from radio searches of dSphs relative to the results presented here: mapping larger, offset fields (§4.4.1), carrying out a joint analysis of a large sample (§4.4.2), and exploring a variety of WIMP annihilation models (§4.4.3).

##### 4.4.1. Mapping Larger, Offset dSph Fields

While the constraints on  $\langle\sigma v\rangle_\chi$  from CPU07’s “set #2” models and our data are competitive with those from the two-year Fermi-LAT data, the limits from “set #1” are considerably weaker (§4.1). As explained in §3.3, this is due in part to the filtering effect of our baselining procedure on predicted halos with sizes comparable to the map size. This effect can be mitigated by mapping larger regions around each dSph: comparing the input and processed halo profiles derived in §3.3, we estimate that maps extending to  $\sim 20$  half-light radii  $r_h$  (Table 1) would be sufficient to mitigate the filtering of flux from CPU07’s “set #1” prediction, and thus throughout the diffusion model parameter space relevant to the dSphs (§4.1.1). In the extreme case of “set #1” and the UMaII field, the larger maps proposed here would increase our sensitivity of  $\langle\sigma v\rangle_\chi$  by  $\sim 50\%$  (c.f. Fig. 9). While costly in observing time (c.f. Table 2), obtaining larger maps for several dSphs is nonetheless feasible with the GBT.

For example, we estimate that a  $6^\circ \times 6^\circ$  map of the same quality as those presented here – which would probe the radio halo of Draco out to  $\sim 20r_h$  – could be obtained with the GBT in  $\sim 30$  hours.

As also discussed in §3.3, it is advantageous to offset the fields relative to the dSph centroids in order to minimize the curvature about the map center introduced by our baselining procedure. In the particular case of Draco, we estimate that an offset of  $\sim 5r_h$  is sufficient, with the added bonus of probing even farther into the putative halo of this dSph on one side. We note that larger, offset maps of Draco and Coma represent the most promising approach for mitigating the limitations imposed by foregrounds in the present study (c.f. §4.2), since in the absence of curvature bias (c.f. §3.3), foregrounds and annihilation halos should have different spatial distributions.

#### 4.4.2. A Larger Sample of dSphs

In analogy to joint dSph analyses at  $\gamma$ -ray energies (Ackermann et al. 2011; Geringer-Sameth & Koushiappas 2011), we anticipate that combining subtracted Stokes I maps for several dSph fields will improve our constraints on  $\langle\sigma v\rangle_\chi$ . The sensitivity of our subtracted maps is limited by both systematic mapping errors and Galactic foregrounds ( $\sigma_{map}$  and  $\sigma_{ast}$  in Table 3, respectively): particularly because of the latter issue (c.f. §4.2), it is unlikely that deeper observations of a single target will improve upon the  $\langle\sigma v\rangle_\chi$  limits presented here. However, our constraint on  $\langle\sigma v\rangle_\chi$  should tighten when a larger sample of dSphs is jointly considered, enabling detailed, simultaneous modelling of extended annihilation halos and the Galactic foreground (c.f. §4.2.2). There is certainly potential for enlarging the dSph sample presented here with additional GBT observations: all but one of the 10 dSphs considered by Ackermann et al. (2011) are accessible to the GBT, as are several other Galactic dSphs from the recent compilation of McConnachie (2012).

A compromise between sample size and telescope time investment would be to target the subset of accessible dSphs with the highest predicted annihilation fluxes. In the particular case of the GBT, we estimate that a 150-hour survey program could obtain maps extending to  $\sim 20r_h$  of the dSphs with the brightest putative radio halos, with J-values in the range  $18.4 \lesssim \log(J, \text{GeV cm}^{-5}) \lesssim 19.6$  (Ackermann et al. 2011; see also Charbonnier et al. 2011): Segue 1, UMaII, Coma, Draco, Ursa Minor, and Sculptor. We expect to be able to map all of these high-latitude fields to the same sensitivity as achieved in this paper. This sample is a good fit for the GBT, since other potential targets are expected to be an order of magnitude fainter than this lower bound (Ackermann et al. 2011). It is therefore feasible to nearly double the size of the sample considered here, while also obtaining sufficiently large maps to mitigate the filtering and curvature bias effects of our baselining procedure. Optimistically, one would hope to constrain  $\langle\sigma v\rangle_\chi$  in these 6 systems, thus tripling the number of targets analysed in this paper and enabling a joint foreground-annihilation halo analysis.

#### 4.4.3. Detailed dSph and WIMP Models

As emphasized in §4.1.1, our comparisons to the CPU07 models in Fig. 1 – particularly their “set #2” – are sufficient to estimate the magnitude of  $\langle\sigma v\rangle_\chi$  probed by our maps. Recall, however, that the models considered here adopt a single WIMP mass ( $M_\chi = 100 \text{ GeV}$ ) and magnetic field strength ( $B = 1 \mu\text{G}$ ), and only two sets of diffusion parameters (“set #1” and “set #2”). Our deep radio observations therefore afford a more sophisticated analysis than the preliminary work presented here. In particular, our upper limits could be refined through comparisons to a suite of predictions that span the expected parameter space for dSph diffusion models, and incorporate J-values and their uncertainties appropriate for each dSph. A preliminary application of such predictions to our UMaII data indicates that the resulting constraints on  $\langle\sigma v\rangle_\chi$  are comparable to the “set #2” results presented here (A. Natarajan et al., in preparation). Together with an exploration of different decay channels and  $M_\chi$ , a detailed set of models would afford a thorough investigation of the range of  $\langle\sigma v\rangle_\chi$  that are allowed by our data given different assumptions about both dSph and WIMP properties.

## 5. CONCLUSIONS

Models by CPU07 predict that for plausible values of the turbulent magnetic field strength and charged particle propagation parameters in the Draco dSph, WIMP annihilations in its dark matter halo will produce a degree-scale synchrotron radio halo that is accessible to current single-dish facilities. We present deep GBT observations at 1.4 GHz of a total of  $40.5^\circ$  around the Draco, UMaII, Coma, and Will1 dSphs to detect this annihilation signature.

We search for extended radio emission associated with the dSphs at sensitivities  $\sigma_{sub} \lesssim 7 \text{ mJy/beam}$  (§2.1) by subtracting discrete sources in the Stokes I maps using the NVSS catalog. The subtracted map noise is not limited by our discrete source subtraction; it is therefore possible to map well below the nominal confusion limit with the GBT when the NVSS is used to remove background sources. We obtained near-concurrent observations of the Draco field with the VLA (§2.2), and use them to demonstrate that variability in the discrete source population has a negligible impact on our results (§3.2).

For each subtracted Stokes I map, we compute radial profiles about the dSph at the map center, jackknifing the data in observation time, telescope elevation and telescope PA to determine robust uncertainties on each profile point (§3.1). We find that  $I(r) \neq 0$  with high significance in the Draco and Coma fields. The depression in the Coma field almost certainly stems from foregrounds. While the emission profile computed from the Draco field resembles that expected for an extended halo, several lines of evidence suggest that it too stems from foregrounds (§4.1.2). Indeed, our subtracted maps probe foregrounds at unprecedented sensitivity and resolution (§4.2): we find that the standard deviation in our maps attributable to foregrounds is  $1.8 \text{ mJy/beam} \leq \sigma_{ast} \leq 5.7 \text{ mJy/beam}$ , where  $\sigma_{ast}$  roughly anti-correlates with the galactic latitude range  $35^\circ \leq b \leq 84^\circ$  of the maps. Because of their strong foreground contamination, we do not attempt to constrain  $\langle\sigma v\rangle_\chi$  from the Draco or Coma fields.

We find no statistically significant features in the UMaII and Will1 profiles, suggesting that these fields are devoid of both foreground contamination and WIMP annihilations. Assuming that the emission from a putative radio halo in these dSphs is consistent with zero, we use the uncertainties on the profile points in those fields to place limits on the annihilation cross-section  $\langle\sigma v\rangle_\chi$  in the context of the CPU07 models for Draco (§4.1.1), which we scale radially according to the stellar distribution sizes of the other dSphs. We compare the fiducial CPU07 models with  $M_\chi = 100$  GeV annihilating into  $b\bar{b}$  final states,  $B = 1 \mu\text{G}$  and two sets of charged particle propagation parameters, and account for the filtering of those models by our baselining procedure (§3.3). We argue that CPU07’s “set #2” model is most appropriate for dSphs, and that the resulting annihilation flux predictions are likely valid to within an order of magnitude.

In the context of the CPU07 models, our upper limits from the UMaII and Will fields imply  $\log(\langle\sigma v\rangle_\chi, \text{cm}^3 \text{s}^{-1}) \lesssim -25$  for the preferred “set #2” propagation parameters (§4.1.1). This constraint is comparable to the limits for individual dSphs obtained at  $\gamma$ -ray energies from the two-year Fermi-LAT data. We discuss three potential avenues for improving the limits

on  $\langle\sigma v\rangle_\chi$  from deep radio observations: mapping larger fields that are offset from the dSph optical centroids (§4.4.1), carrying out a joint analysis of a larger sample of dSphs (§4.4.2), and applying a more sophisticated suite of models to the data (§4.4.3). We therefore conclude that deep radio observations are highly complementary to indirect WIMP searches at higher energies, and have the potential to probe  $\langle\sigma v\rangle_{\chi,th}$  expected for a thermal relic.

The National Radio Astronomy Observatory is a facility of the National Science Foundation operated under cooperative agreement by Associated Universities, Inc. This project was initiated while K. S. and J. A. were Jansky Fellows of the National Radio Astronomy Observatory. K. S. acknowledges support from the National Science and Engineering Research Council of Canada. We thank S. Srikanth for providing the GBT  $\nu = 1.4$  GHz beam model used in this analysis, A. Natarajan for helpful discussions regarding WIMP annihilation models and the anonymous referee whose comments helped clarify the interpretation of our data.

*Facilities:* NRAO: GBT, VLA

## REFERENCES

- Abazajian, K. N. & Harding, J. P. 2012, JCAP, 1, 41  
 Abazajian, K. N. & Kaplinghat, M. 2012, Phys. Rev. D, 86, 083511  
 Abdo, A. A. et al. 2010a, Physical Review Letters, 104, 091302  
 —. 2010b, ApJ, 712, 147  
 —. 2010c, JCAP, 4, 14  
 Abramowski, A. et al. 2012, ApJ, 750, 123  
 Ackermann, M. et al. 2011, Physical Review Letters, 107, 241302  
 —. 2010, JCAP, 5, 25  
 —. 2012a, ArXiv e-prints  
 —. 2012b, ApJ, 755, 164  
 Aguirre, J. E. et al. 2011, ApJS, 192, 4  
 Aleksić, J. et al. 2011, JCAP, 6, 35  
 Aliu, E. et al. 2012, Phys. Rev. D, 85, 062001  
 Ando, S. & Nagai, D. 2012, JCAP, 7, 17  
 Atwood, W. B. et al. 2009, ApJ, 697, 1071  
 Baxter, E. J. & Dodelson, S. 2011, Phys. Rev. D, 83, 123516  
 Beck, R. 2011, ArXiv e-prints  
 Beck, R. & Krause, M. 2005, Astronomische Nachrichten, 326, 414  
 Becker, R. H., White, R. L., & Helfand, D. J. 1995, ApJ, 450, 559  
 Bennett, C. L. et al. 2003, ApJS, 148, 1  
 Bergström, L. 2000, Reports on Progress in Physics, 63, 793  
 Bergström, L., Fairbairn, M., & Pieri, L. 2006, Phys. Rev. D, 74, 123515  
 Borriello, E., Longo, G., Miele, G., Paolillo, M., Siffert, B. B., Tabatabaei, F. S., & Beck, R. 2010, ApJ, 709, L32  
 Calura, F., Lanfranchi, G. A., & Matteucci, F. 2008, A&A, 484, 107  
 Charbonnier, A. et al. 2011, ArXiv e-prints  
 Chyży, K. T., Beck, R., Kohle, S., Klein, U., & Urbanik, M. 2000, A&A, 355, 128  
 Chyży, K. T., Knapik, J., Bomans, D. J., Klein, U., Beck, R., Soida, M., & Urbanik, M. 2003, A&A, 405, 513  
 Chyży, K. T., Weżgowiec, M., Beck, R., & Bomans, D. J. 2011, A&A, 529, A94+  
 Cirelli, M., Panci, P., & Serpico, P. D. 2010, Nuclear Physics B, 840, 284  
 Colafrancesco, S., Profumo, S., & Ullio, P. 2006, A&A, 455, 21  
 —. 2007, Phys. Rev. D, 75, 023513  
 Condon, J. J. 1974, ApJ, 188, 279  
 Condon, J. J., Cotton, W. D., Greisen, E. W., Yin, Q. F., Perley, R. A., Taylor, G. B., & Broderick, J. J. 1998, AJ, 115, 1693  
 Crocker, R. M., Bell, N. F., Balázs, C., & Jones, D. I. 2010, Phys. Rev. D, 81, 063516  
 Croft, S. et al. 2010, ApJ, 719, 45  
 de Oliveira-Costa, A., Tegmark, M., Gaensler, B. M., Jonas, J., Landecker, T. L., & Reich, P. 2008, MNRAS, 388, 247  
 de Vries, W. H., Becker, R. H., White, R. L., & Helfand, D. J. 2004, AJ, 127, 2565  
 Dicker, S. R. et al. 2009, ApJ, 705, 226  
 Dobler, G., Cholis, I., & Weiner, N. 2011, ApJ, 741, 25  
 Dobler, G., Finkbeiner, D. P., Cholis, I., Slatyer, T., & Weiner, N. 2010, ApJ, 717, 825  
 Donato, F., Fornengo, N., Maurin, D., Salati, P., & Taillet, R. 2004, Phys. Rev. D, 69, 063501  
 Feng, J. L. 2010, ARA&A, 48, 495  
 Fomalont, E. B. & Geldzahler, B. J. 1979, AJ, 84, 12  
 Fornengo, N., Lineros, R. A., Regis, M., & Taoso, M. 2012, JCAP, 1, 5  
 Gaensler, B. M., Haverkorn, M., Staveley-Smith, L., Dickey, J. M., McClure-Griffiths, N. M., Dickel, J. R., & Wolleben, M. 2005, Science, 307, 1610  
 Gallagher, J. S., Madsen, G. J., Reynolds, R. J., Grebel, E. K., & Smecker-Hane, T. A. 2003, ApJ, 588, 326  
 Geringer-Sameth, A. & Koushiappas, S. M. 2011, Physical Review Letters, 107, 241303  
 Gregorini, L., Ficarra, A., & Padrielli, L. 1986, A&A, 168, 25  
 Greisen, E. W. 2003, Information Handling in Astronomy - Historical Vistas, 285, 109  
 Han, J., Frenk, C. S., Eke, V. R., Gao, L., White, S. D. M., Boyarsky, A., Malyshev, D., & Ruchayskiy, O. 2012, MNRAS, 427, 1651  
 Haslam, C. G. T., Salter, C. J., Stoffel, H., & Wilson, W. E. 1982, A&AS, 47, 1  
 Hooper, D. 2008, Phys. Rev. D, 77, 123523  
 Hooper, D., Belikov, A. V., Jeltema, T. E., Linden, T., Profumo, S., & Slatyer, T. R. 2012, Phys. Rev. D, 86, 103003  
 Hooper, D., Finkbeiner, D. P., & Dobler, G. 2007, Phys. Rev. D, 76, 083012  
 Inoue, Y. 2011, ApJ, 733, 66  
 Jeltema, T. E. & Profumo, S. 2008, ApJ, 686, 1045  
 Jungman, G., Kamionkowski, M., & Griest, K. 1996, Phys. Rep., 267, 195  
 Kepley, A., Zweibel, E., Wilcots, E., Johnson, K., & Robishaw, T. 2011, ArXiv e-prints  
 Kepley, A. A., Mühle, S., Everett, J., Zweibel, E. G., Wilcots, E. M., & Klein, U. 2010, ApJ, 712, 536  
 Klein, U., Wielebinski, R., Haynes, R. F., & Malin, D. F. 1989, A&A, 211, 280  
 Komatsu, E. et al. 2011, ApJS, 192, 18



- Laha, R., Ng, K. C. Y., Dasgupta, B., & Horiuchi, S. 2012, ArXiv e-prints
- Linden, T., Profumo, S., & Anderson, B. 2010, *Phys. Rev. D*, 82, 063529
- Martin, N. F., de Jong, J. T. A., & Rix, H.-W. 2008, *ApJ*, 684, 1075
- Mateo, M. L. 1998, *ARA&A*, 36, 435
- Matsumura, N. et al. 2009, *AJ*, 138, 787
- Maurin, D., Donato, F., Taillet, R., & Salati, P. 2001, *ApJ*, 555, 585
- Mayer, L. 2010, *Advances in Astronomy*, 2010
- McConnachie, A. W. 2012, *AJ*, 144, 4
- Muñoz, R. R., Geha, M., & Willman, B. 2010, *AJ*, 140, 138
- Oppermann, N. et al. 2012, *A&A*, 542, A93
- Papucci, M. & Strumia, A. 2010, *JCAP*, 3, 14
- Pérez-Torres, M. A., Zandanel, F., Guerrero, M. A., Pal, S., Profumo, S., Prada, F., & Panessa, F. 2009, *MNRAS*, 396, 2237
- Planck Collaboration et al. 2011, *A&A*, 536, A21
- Porter, T. A., Johnson, R. P., & Graham, P. W. 2011, ArXiv e-prints
- Profumo, S. & Ullio, P. 2010, ArXiv e-prints
- Siffert, B. B., Limone, A., Borriello, E., Longo, G., & Miele, G. 2011, *MNRAS*, 410, 2463
- Storm, E., Jeltema, T. E., Profumo, S., & Rudnick, L. 2012, ArXiv e-prints
- Strigari, L. E. 2012, ArXiv e-prints
- Strigari, L. E., Koushiappas, S. M., Bullock, J. S., & Kaplinghat, M. 2007, *Phys. Rev. D*, 75, 083526
- Strigari, L. E., Koushiappas, S. M., Bullock, J. S., Kaplinghat, M., Simon, J. D., Geha, M., & Willman, B. 2008, *ApJ*, 678, 614
- Su, M., Slatyer, T. R., & Finkbeiner, D. P. 2010, *ApJ*, 724, 1044
- Tasitsiomi, A., Gaskins, J., & Olinto, A. V. 2004, *Astroparticle Physics*, 21, 637
- Walker, M. G., Combet, C., Hinton, J. A., Maurin, D., & Wilkinson, M. I. 2011, *ApJ*, 733, L46
- Weisz, D. R. et al. 2011, ArXiv e-prints
- Weniger, C. 2012, *JCAP*, 8, 7
- White, R. L., Becker, R. H., Helfand, D. J., & Gregg, M. D. 1997, *ApJ*, 475, 479